


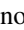
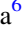

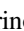










Long-term Variations of Venus's 365 nm Albedo Observed by *Venus Express*, *Akatsuki*, *MESSENGER*, and the *Hubble Space Telescope*

Yeon Joo Lee^{1,17} , Kandis-Lea Jessup², Santiago Perez-Hoyos³ , Dmitrij V. Titov⁴ , Sebastien Lebonnois⁵ , Javier Peralta⁶ , Takeshi Horinouchi⁷ , Takeshi Imamura¹ , Sanjay Limaye⁸, Emmanuel Marcq⁹ , Masahiro Takagi¹⁰ , Atsushi Yamazaki^{6,11} , Manabu Yamada¹² , Shigeto Watanabe¹³, Shin-ya Murakami⁶ , Kazunori Ogohara¹⁴ , William M. McClintock¹⁵,

Gregory Holsclaw¹⁵, and Anthony Roman¹⁶

¹ Graduate School of Frontier Sciences, The University of Tokyo, Kashiwa, Japan; yjleeinjanpan@gmail.com

² Southwest Research Institute, Boulder, CO, USA

³ Departamento Física Aplicada I, Escuela de Ingeniería, Universidad del País Vasco UPV/EHU, Bilbao, Spain

⁴ ESTEC/ESA, Noordwijk, Netherlands

⁵ LMD/IPSL, CNRS, Paris, France

⁶ Institute of Space and Astronautical Science (ISAS/JAXA), Sagami, Japan

⁷ Faculty of Environmental Earth Science, Hokkaido University, Sapporo, Japan

⁸ Space Science and Engineering Center, University of Wisconsin, Madison, WI, USA

⁹ LATMOS/IPSL, UVSQ Université Paris-Saclay, Sorbonne Université, CNRS, Guyancourt, France

¹⁰ Department of Astrophysics and Atmospheric Science, Faculty of Science, Kyoto Sangyo University, Kyoto, Japan

¹¹ Department of Earth and Planetary Science, Graduate School of Science, The University of Tokyo, Tokyo, Japan

¹² Planetary Exploration Research Center (PERC), Chiba, Institute of Technology, Narashino, Japan

¹³ Hokkaido Information University, Ebetsu, Japan

¹⁴ University of Shiga Prefecture, Hikone, Japan

¹⁵ Laboratory for Atmospheric and Space Physics, Boulder, CO, USA

¹⁶ Space Telescope Science Institute, Baltimore, MD, USA

Received 2019 March 29; revised 2019 July 9; accepted 2019 July 9; published 2019 August 26

Abstract

An unknown absorber near the cloud-top level of Venus generates a broad absorption feature from the ultraviolet (UV) to visible, peaking around 360 nm, and therefore plays a critical role in the solar energy absorption. We present a quantitative study of the variability of the cloud albedo at 365 nm and its impact on Venus's solar heating rates based on an analysis of *Venus Express* and *Akatsuki* UV images and *Hubble Space Telescope* and *MESSENGER* UV spectral data; in this analysis, the calibration correction factor of the UV images of *Venus Express* (Venus Monitoring Camera) is updated relative to the *Hubble* and *MESSENGER* albedo measurements. Our results indicate that the 365 nm albedo varied by a factor of 2 from 2006 to 2017 over the entire planet, producing a 25%–40% change in the low-latitude solar heating rate according to our radiative transfer calculations. Thus, the cloud-top level atmosphere should have experienced considerable solar heating variations over this period. Our global circulation model calculations show that this variable solar heating rate may explain the observed variations of zonal wind from 2006 to 2017. Overlaps in the timescale of the long-term UV albedo and the solar activity variations make it plausible that solar extreme UV intensity and cosmic-ray variations influenced the observed albedo trends. The albedo variations might also be linked with temporal variations of the upper cloud SO₂ gas abundance, which affects the H₂SO₄–H₂O aerosol formation.

Key words: planets and satellites: atmospheres – planets and satellites: individual (Venus) – planets and satellites: terrestrial planets

1. Introduction

The solar radiance is the principal energy source for the atmosphere of terrestrial planets, such as Earth, Venus, and Mars. Inhomogeneous solar radiance absorption drives atmospheric motions, from small-scale convection to large-scale global circulation. These motions distribute excess energy and transport mass and momentum in the atmosphere. Temporal variation of absorbed solar radiance is therefore an important indication of possible changes in the atmosphere. The long-term monitoring of solar energy absorption is particularly

useful in radiative energy balance calculations as a major input energy into a planetary system.

On the atmosphere of Venus, the maximum solar energy deposition occurs in the upper cloud layer (60–70 km) rather than at the surface, as in the case of the Earth (Crisp 1986; Titov et al. 2012). The maximum solar energy absorption in the clouds is due to an unidentified absorber, hereafter called the “unknown absorber,” which has been an unsolved question in Venus research regarding its identity. Venus's global-scale clouds and upper haze are mainly composed of H₂SO₄–H₂O (Allen 1964; Mills et al. 2007; Titov et al. 2012), which has a small imaginary refractive index ($n_i = [1-9] \times 10^{-8}$) in the UV-to-visible range (Palmer & Williams 1975; Hummel et al. 1988). As a result, the H₂SO₄–H₂O clouds and haze absorb almost none of the solar radiance in this spectral range but are effective scatterers, making a strong contribution to the total solar radiance scattered back to space (which is ~75% of the incident flux; Titov et al. 2012). However, UV images of Venus show distinct patterns caused by the unknown absorber. The absorption spectrum produced by the

¹⁷ current e-mail: y.j.lee@astro.physik.tu-berlin.de, current affiliation: Zentrum für Astronomie und Astrophysik, Technische Universität Berlin, Hardenbergstr. 36, 10623 Berlin, Germany.

unknown absorber is observed to reach maximum absorption levels between 340 and 380 nm and then decrease smoothly with increasing wavelength from 380 nm through the visible range (Barker et al. 1975; Pérez-Hoyos et al. 2018). Some studies indicate that an absorption tail exists at wavelengths shortward of 340 nm (Pérez-Hoyos et al. 2018) and in the 170–320 nm range (Marcq et al. 2011). According to data from descent probes, the unknown absorber may be located in the upper clouds (Esposito 1980; Tomasko et al. 1980) and absorbs about half of the solar radiance deposited at the cloud-top level, accounting for ~ 3 K Earth day⁻¹ of the global mean solar heating around 65 km altitude, when the total global mean solar heating is ~ 6 K day⁻¹ (Crisp 1986). Many candidates have been proposed for the unknown absorber, including OSSO, S₂O, S_x, FeCl₃, and iron-bearing microorganisms (Mills et al. 2007; Frandsen et al. 2016; Krasnopolsky 2017; Limaye et al. 2018; Pérez-Hoyos et al. 2018). However, none of the non-microorganism species satisfy all of the spectral features produced by the unknown absorber, and the lifetime and simulated vertical profile required to fit the observations (Krasnopolsky 2018; Pérez-Hoyos et al. 2018). In addition, the microorganism species have not been compared with the observations nor simulations (Limaye et al. 2018).

The UV patterns reveal clear temporal variations, for example, 4–5 days in the UV reflectivity (Del Genio and Rossow 1982; Lee et al. 2015a) that is caused by a combination of the well-known strong zonal winds, or “superrotation,” rotating around the globe in 4–5 days (Rossow et al. 1990; Kouyama et al. 2013) and Venus’s infamous “Y-feature,” which is explained with atmospheric waves, resulting in a short-term periodicity of 4–5 days (Boyer & Camichel 1961; Limaye & Soumi 1981; Del Genio & Rossow 1982, 1990; Kouyama et al. 2015; Peralta et al. 2015; Imai et al. 2016). In the meantime, long-term variations are also reported in the cloud-tracked wind speeds (Khatuntsev et al. 2013; Kouyama et al. 2013), in mesospheric SO₂ gas abundance (Marcq et al. 2013), and in latitudinal UV contrasts (Lee et al. 2015a). Temporal variations of the latitudinal 365 nm contrasts are closely linked with the SO₂ gas abundance above the cloud-top level (Lee et al. 2015a), suggesting influences of chemical processes on sulfuric acid cloud aerosol formations in the UV contrast (Esposito & Travis 1982; Parkinson et al. 2015). Since Marcq et al. (2013) reported a general decline in the SO₂ gas abundance in the same periods where a decline in the long-term 365 nm cloud-top albedo was observed, Lee et al. (2015a) proposed that the rate of H₂SO₄ production, dependent on SO₂ photolysis, may be the principal mechanism supporting the observed long-term 365 nm albedo variation trends. However, definitive claims regarding these relationships were not made by Lee et al. (2015a) due to uncertainties at that time regarding the impact of the instrument degradation on the retrieved 365 nm cloud-top albedo (Shalygina et al. 2015).

In this study, we report that the long-term variations of the UV reflectivity are a real phenomenon through a comparison of four space-based instruments: imagers on board *Venus Express* and *Akatsuki* and spectrometers on board the *MERCURY Surface, Space ENvironment, Geochemistry, and Ranging (MESSENGER)* and the *Hubble Space Telescope (HST)* (Section 2). We carefully check the same phase angle disk-resolved data (Section 3.1.2) and update the calibration correction factor of the UV data of *Venus Express* through a cross-comparison with the UV spectra of *MESSENGER* and *HST* (Section 3.1.4). We evaluate the updated UV image data of *Venus Express* by a comparison of whole-disk

albedo (Section 3.2) with the UV images of *Akatsuki*, showing a successful performance. We find common long-term variations in both the disk-resolved and whole-disk albedo (Sections 4.1 and 4.2). The results are employed in our radiative transfer model calculations to understand possible solar heating variations (Sections 3.3 and 4.3). We discuss the significance of these results for the relationship with atmospheric winds at the cloud-top level, including Venus global circulation model calculations, and possible reasons for the observed 365 nm albedo variations in Section 5.

2. Data

Our 365 nm reflectivity analysis covers a period of a decade, from 2006 to 2017, with only a 1 yr gap in 2015. The data were acquired from four instruments. The longest period of monitoring, 2006–2014, was covered with the Venus Monitoring Camera (VMC) on board *Venus Express* (Markiewicz et al. 2007). Two sets of 365 nm images were taken with the UV Imager (UVI) on board *Akatsuki*; one set of images was acquired from a far distance in 2011 after the first Venus orbit insertion failure of *Akatsuki* (Nakamura et al. 2014), and the other set of images was taken from 2015 December to 2017 May after the successful orbit insertion (Nakamura et al. 2016). Regular star observations for UVI have been conducted since 2010 for calibration purposes. This revealed steady sensitivity over time (Yamazaki et al. 2018), and the mean error range in 2010–2017 was 18%. Near-UV spectra were taken with the Mercury Atmospheric and Surface Composition Spectrometer (MASCS) on board *MESSENGER* during its Venus flyby on 2007 June 5 using the VIS-VIRS channel (320–950 nm, spectral resolution 4.7 nm; Pérez-Hoyos et al. 2018). An error of 5%–10% is estimated at 340–390 nm from star observations during *MESSENGER*’s cruise phase (Holsclaw et al. 2010). Other near-UV Venus spectra were taken with the Space Telescope Imaging Spectrograph (STIS) of *HST* with the G430L grating mode (290–570 nm, spectral resolution 0.54 nm) on 2011 January 2 (Jessup et al. 2015). A 5% error is estimated for STIS measurements based on regular standard-star observations (Jessup et al. 2019).

The MASCS in 2007, and STIS and UVI in 2011 data overlap observations with VMC data in 2007 and 2011. This is important for radiometric comparisons, as all three performed star observations and retrieved radiometric uncertainties independently. The VMC data are highly uncertain in terms of radiometric calibration, as the star observations revealed an 82% error (Titov et al. 2012; Shalygina et al. 2015). Cross-calibration between the VMC and the Visible and Infrared Thermal Imaging Spectrometer (VIRTIS) on board *Venus Express* was conducted using simultaneous overlapped spectral range observations between VIRTIS and the VMC (Titov et al. 2012; Shalygina et al. 2015). However, the absolute calibration of VIRTIS was not available at the time of these publications, resulting in questions about this cross-calibration (Lee et al. 2015a). Comparisons in our study show that this VMC and VIRTIS cross-calibration factor and the retrieved sensitivity degradation ratio of the 365 nm filter results in too large a difference in the VMC data with respect to MASCS, STIS, and UVI (Section 3.1.4). This will be discussed in detail (Section 3).

The VMC images were manually selected in order to filter out those exhibiting artifacts, which could not be successfully corrected with additional flat-field corrections (Titov et al. 2012). In addition, we selected VMC and UVI images having the dayside of Venus completely within the field of view. There

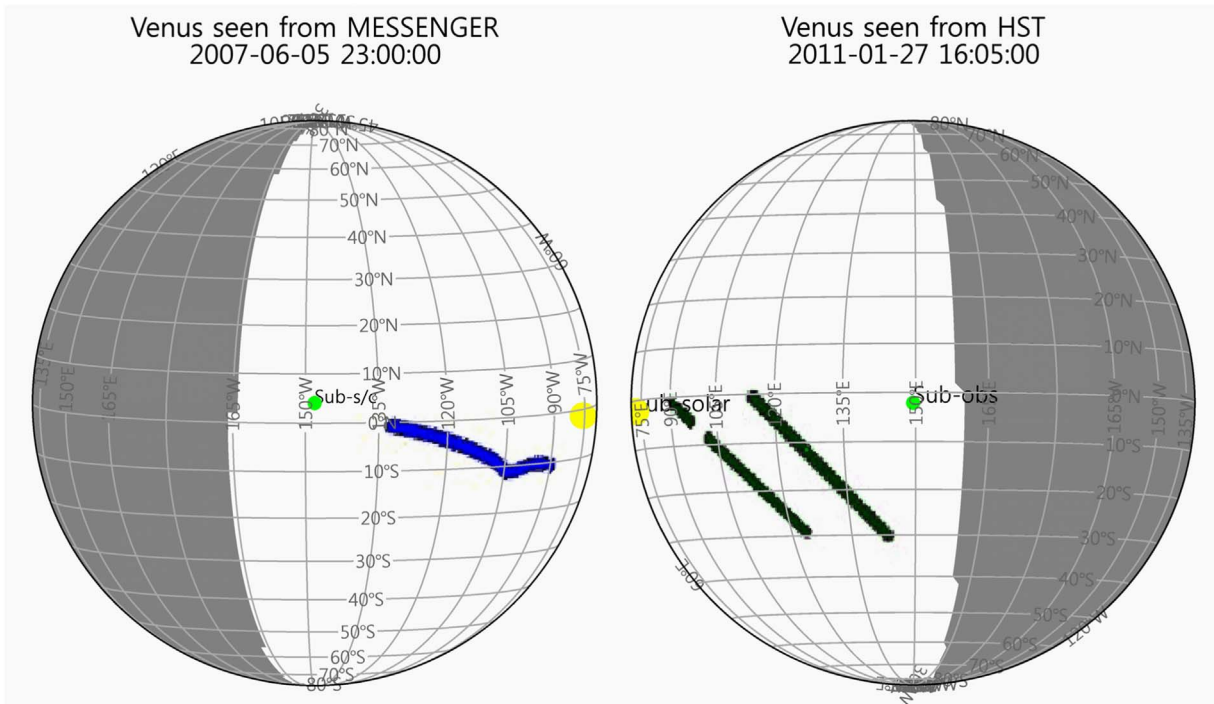


Figure 1. Viewing geometries of spectral data. (Left) MASCS on 2007 June 5 at 72° of spacecraft center of the Venus–Sun (phase) angle position. The blue data points were acquired at the 85° – 90° phase angles following the progress of the spacecraft during its flyby. (Right) STIS on 2011 January 27 as seen at 79° phase angle. White is dayside, and the shaded area is nightside. Blue and dark green filled symbols indicate spectral data locations. Yellow symbols are subsolar points, and light green symbols are a sub-*MESSENGER* and sub-Earth at the time indicated at the top of the panels in UTC.

Table 1
Summary of 365 nm Observations Used in This Study

Instrument Filter or Channel	VMC	UVI		MASCS	STIS
	365 nm	365 nm		VIS-VIRS	G430L
Date	2006 May –2014 May	2011 February –May	2015 December –2017 May	2007 June 5	2011 January 27
Number of images/spectra	17,742	82	1619	152	45
Phase angle [deg]	52.3–138.6	0.9–62.9	0.9–144.0	89.7–90.0	79.3
Latitude [deg]	Southern hemisphere	N and S	N and S, or Southern	0–30S	0–30S
Longitude [deg E]	0–360	135–(360)–75	0–360	75–148	91–144

are two UVI flat fields of the CCD matrix, and this study used the one measured on the ground before the launch of *Akatsuki* (Yamazaki et al. 2018). The same data were used for the star flux calibration (Yamazaki et al. 2018), and the mean calibration correction factor (β) was 1.525 in 2010–2017. We multiplied this calibration correction factor β by the measured radiance of UVI. The other UVI flat-field data were made with the onboard diffuser, and the public data in DARTS and PDS were generated using the onboard diffuser flat field.

Except for the VMC, which mostly observed the southern hemisphere (Titov et al. 2012), the other three instruments observed both the northern and southern hemispheres. For disk-resolved data, our comparison is done only for the southern hemisphere, keeping the consistency with VMC data (see Section 3.1.3). Since 365 nm images show persistent dark low latitudes and bright high latitudes (Figure 2), we compare low (0° – 30°) and high (50° – 70°) latitudes separately for all images. Spectral data were taken using a narrow slit and observed Venus across from local noon toward the terminator of a half-illuminating phase, as shown in Figure 1. All spectral data sets

fall into low- and middle- (30° – 50°) latitudinal bins, and we use only the southern low-latitude bin data in this study. For disk integration (Section 3.2), we did not distinguish hemispheres, and we used all valid pixels on the Venus disk. Table 1 shows the configurations of the four data sets used in this study.

3. Methods

For disk-resolved images, we calculated a radiance factor (Hapke 2012 and Section 3.1.1) and then the albedo, applying photometric correction (Section 3.1.2). Spectral data were convolved using the filter transmittance function of the 365 nm channel of VMC, and we applied the same photometric correction as for the images. In order to take into account UVI’s 2011 data, we calculated the whole-disk albedo (Sromovsky et al. 2001; García Muñoz et al. 2014, 2017) without photometric correction due to the small apparent size of Venus (Section 3.2). Radiative transfer model calculations were performed using the model and gaseous database in Lee et al. (2015b, 2016 and Section 3.3) to estimate the abundance

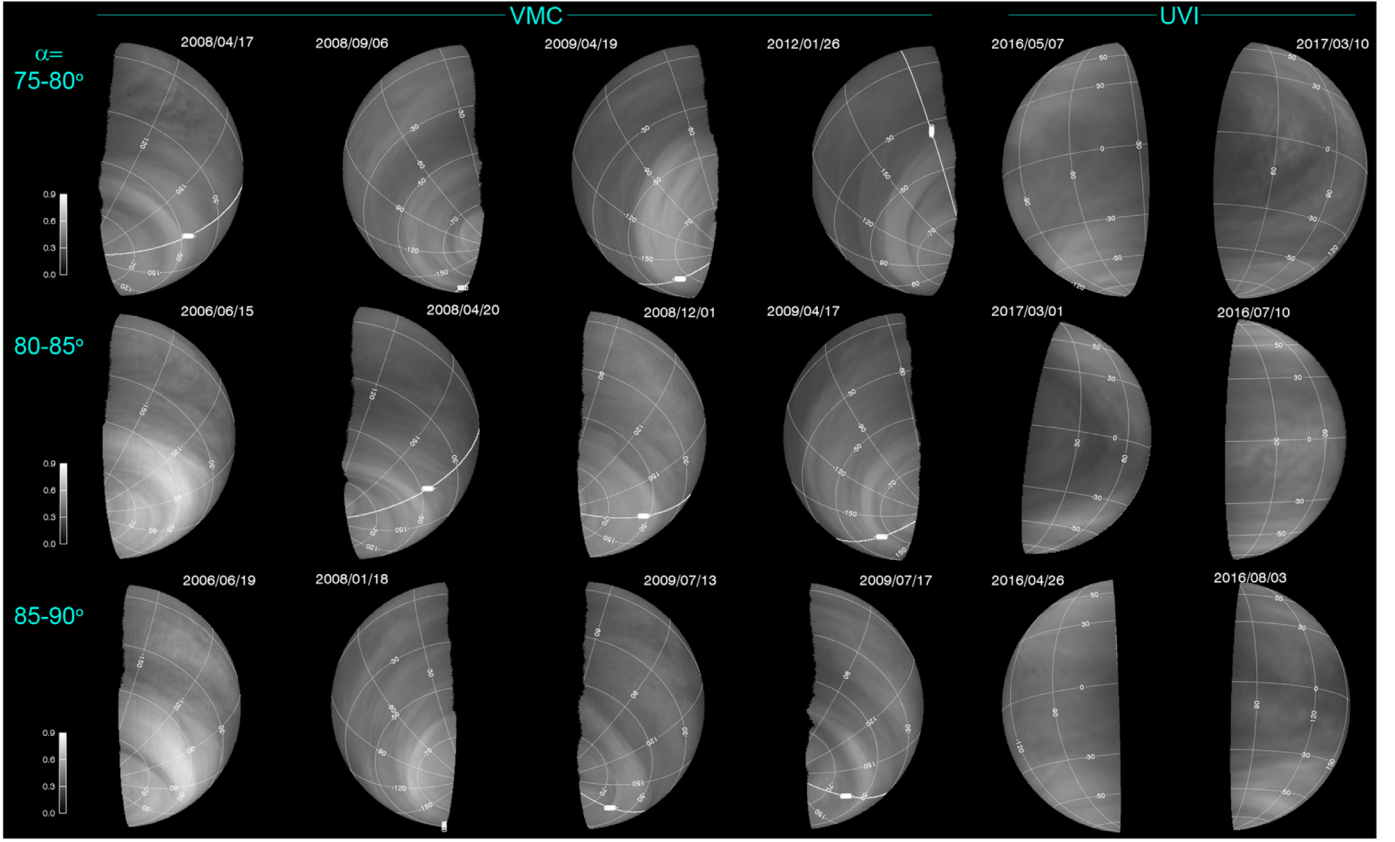


Figure 2. Example 365 nm images of Venus. These present the cloud-top albedo as observed by VMC and UVI between 2006 and 2017, when the observational phase angle was comparable to either STIS or MASCS Venus observations. In these example images, only Venus’s dayside a.m. or p.m. quadrant was visible within the camera field of view. The first row shows images obtained in the 75°–80° phase angle range, the second row images were obtained at 80°–85°, and the third row images were obtained at 85°–90°. The left four columns are images taken by VMC covering latitudes extending from 90°S to ~10°S, and the right two columns are pole-to-pole dayside images obtained by UVI. Though the higher latitudes are brighter in the UVI observations than the equator, the intense polar hood brightening detected at 40–70°S by VMC in 2006 has not been observed by UVI. All images are photometrically corrected (see Section 3.1.2) and share the same color bar on the left.

of the unknown absorber that explains the observed 365 nm albedo and calculate solar heating rates.

3.1. Disk-resolved Albedo

3.1.1. Reflectivity

We converted the observed radiance to a radiance factor, r_F (Hapke 2012), the ratio of bidirectional reflectivity of a surface to the perfectly diffuse Lambertian surface illuminated normally. We calculate the average solar flux at 1 au (Chance & Kurucz 2010) at each of the UV filters of VMC and UVI, S_{\odot} ($\text{W m}^{-2} \mu\text{m}^{-1}$), and the radiance factor as

$$(r_F) = \pi\beta(R_{\text{obs}}) \frac{d_V^2}{S_{\odot}}, \quad (1)$$

where R_{obs} is the observed radiance ($\text{W m}^{-2} \text{sr}^{-1} \mu\text{m}^{-1}$), β is a calibration correction factor of VMC or UVI, and d_V is the distance of Venus to the Sun (in au).

3.1.2. Photometric Corrections

The 365 nm images show a combination of a smooth gradient from the subsolar point to the terminator, and dark features owing to the presence of the unknown absorber. The smooth gradient depends on the incidence (i), emergence (e), and phase (α) angles, which can be described by a photometric

law (disk function), $D(\mu, \mu_0, \alpha)$, where $\mu = \cos(e)$ and $\mu_0 = \cos(i)$. We can separate albedo, $A(\alpha)$, and disk function, $D(\mu, \mu_0, \alpha)$, from the radiance factor (r_F) that is derived from the measured radiance (Shkuratov et al. 2011),

$$r_F = A(\alpha)D(\mu, \mu_0, \alpha). \quad (2)$$

This albedo A , the equigonal albedo, depends on α (Shkuratov et al. 2011).

Previous studies showed that the Lambert and Lommel-Seeliger law (LLS) performs better in describing the gradient depending on geometric angles, compared to the Lambert law and the Minnaert laws (Lee et al. 2015a, 2017). Therefore, in this study, we adopted the LLS (Buratti & Veverka 1983; McEwen 1986),

$$D_{\text{LLS}} = k(\alpha) \frac{2\mu_0}{\mu_0 + \mu} + (1 - k(\alpha))\mu_0, \quad (3)$$

where k is a coefficient depending on α ,

$$k(\alpha) = 0.216004 + 0.00194196 \times \alpha - (2.11589 \times 10^{-5}) \times \alpha^2, \quad (4)$$

and α is in degrees. Equation (4) is updated from Lee et al. (2017), using more images to find the mean condition along the phase angle.

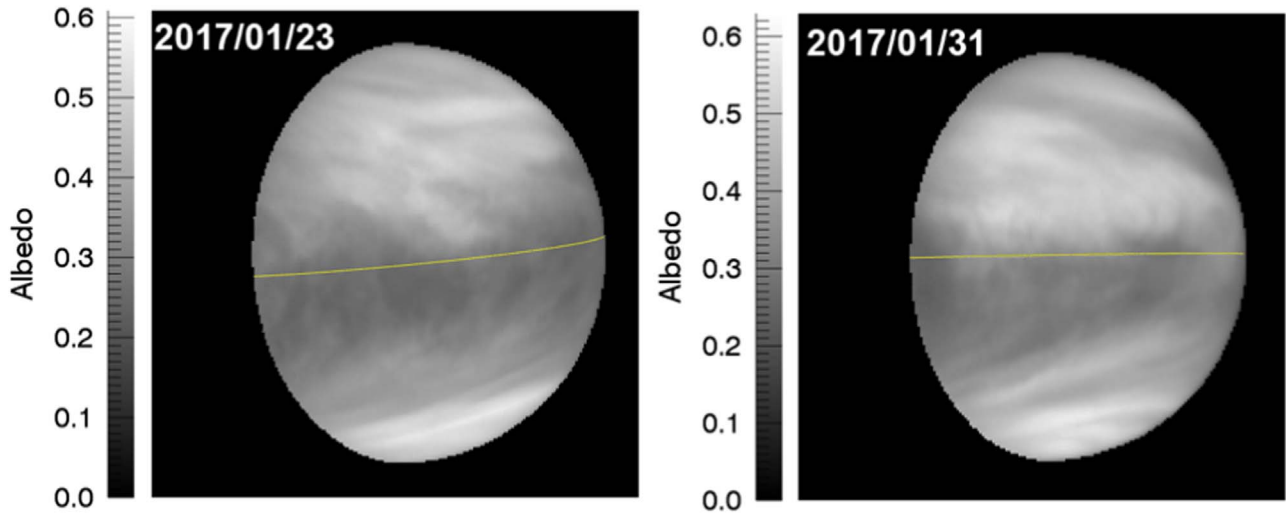


Figure 3. Occasionally appearing hemispheric asymmetry of the 365 nm albedo across the equator, observed on 2017 January 23 (left) and 31 (right) using the UVI on board *Akatsuki*. The yellow line is the equator, and north is up.

3.1.3. Areas of Disk-resolved Albedo for a Comparison

Figure 2 shows albedo A at three 5° phase angle bins: $75^\circ\text{--}80^\circ$, $80^\circ\text{--}85^\circ$, and $85^\circ\text{--}90^\circ$ (top to bottom). The left four columns are VMC images, having middle-latitudinal views close to UVI’s equatorial views in the right two columns. While the UVI data have quality navigation using limb-fitting (Ogohara et al. 2017), the VMC data do not. So, we restricted the VMC data satisfying $i < 84^\circ$, $e < 81^\circ$, and $r_F > 0.05$ (Lee et al. 2015a). The last condition causes a nonsmooth terminator for the VMC images in Figure 2. As shown in these example images, we find no systematic tendency of albedo along local time but temporal variations in the brightness and morphology. We also attempted to search for systematic variations in the albedo along longitude, as the surface topography may affect the 365 nm albedo, particularly over Aphrodite Terra (Bertaux et al. 2016), but the longitudinal coverage of the VMC data is not evenly distributed over time. Additionally, this depends on phase angle selections. A detailed analysis along longitude, latitude, and time requires a different approach from the broad range average utilized in this study. Here we focus on temporal variations using data obtained over a broad range of longitudes. We derive the mean latitudinal albedo from disk-resolved VMC and UVI images, divided into two broad latitude bins: low ($0^\circ\text{--}30^\circ$) and high ($50^\circ\text{--}70^\circ$) latitudes. We also derive a low-latitudinal albedo from the MASCS and STIS spectral data to complete the cross-comparison with the VMC data (Section 3.1.4).

From the equatorial orbit, the UVI images show that cloud-top albedo and contrast patterns primarily displayed north–south symmetry. However, as the example in Figure 3 shows, we also observed cloud-top albedo patterns that were asymmetric across the equator. This asymmetry was observed frequently in 2017 January–February. Wind fields retrieved from cloud motions also detected the similar asymmetry between the northern and southern hemispheres over the same period (Horinouchi et al. 2018). Thus, we restrict our disk-resolved data comparison only for the southern hemisphere, which was observed by all four instruments.

3.1.4. Cross-comparison of Disk-resolved VMC, MASCS, STIS, and UVI Data

The observed long-term decrease of albedo had been previously attributed to the sensitivity degradation of VMC by

Shalygina et al. (2015). Following these authors, we used the 2.32 calibration correction factor (their Figure 12), which was retrieved from the comparison with VIRTIS-IR, and their value for the degradation ratio, k_d ($= -16.2 \times 10^{-5}$ orbit $^{-1}$, and one orbit of *Venus Express* equals 1 Earth day). We correct all VMC data to the value at an initial sensitivity condition (zero orbit number of *Venus Express*) using the equations given in Shalygina et al. (2015),

$$B(t) = B_0(t)\beta, \quad (5)$$

where t is time (orbit); B and B_0 are the corrected and observed radiance, respectively ($\text{W m}^{-2} \text{sr}^{-1} \mu\text{m}^{-1}$); and β is the 2.32 calibration correction factor. The temporal sensitivity degradation correction is given as

$$B(t_2) = B(t_1) \left(\frac{1 + k_d t_2}{1 + k_d t_1} \right), \quad (6)$$

where k_d is the sensor degradation factor (orbit $^{-1}$). We can get $B(t = 0)$ as

$$B(t = 0) = B(t) \left(\frac{1}{1 + k_d t} \right). \quad (7)$$

So the final form is

$$B(t = 0) = B_0(t)\beta \left(\frac{1}{1 + k_d t} \right). \quad (8)$$

Figure 4 shows a comparison of low- and high-latitudinal albedo at the same phase angle bins using the corrected VMC data with Equation (8) (Shalygina et al. 2015). These corrected VMC data are significantly brighter than any of the independently calibrated MASCS, STIS, and UVI observations. The large difference between the 2006 VMC and 2016 UVI is especially noticeable, while the data in 2006 are supposed to have the least sensitivity degradation. We therefore discard this correction on the VMC data due to the inconsistency with other calibrated MASCS, STIS, and UVI data.

Instead, we use the star calibration correction factor, 2.0 ± 0.822 , for the initial calibration correction factor (β) of the 365 nm channel of VMC (Titov et al. 2012; Shalygina et al. 2015). The large error of 82% results in the ambiguous

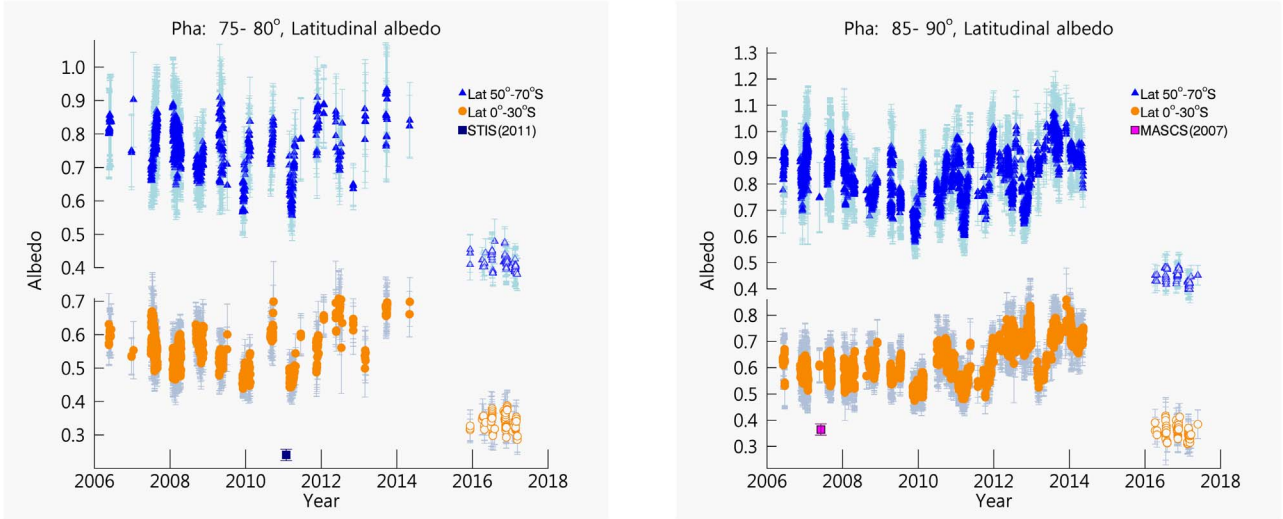


Figure 4. Discarded results on 365 nm albedo comparison. The 365 nm albedo observed by VMC is corrected using Equation (8) (Shalygina et al. 2015; filled symbols). Other 365 nm albedos observed by UVI (open symbols), STIS (navy square), and MASCS (magenta square) are compared. The low- (0–30°S) and high- (50–70°S) latitudinal mean albedo observed at 75°–80° and 85°–90° phase angles are shown in the left and right panels, respectively. Error bars are standard deviations of the albedo.

definition of the absolute radiance. In this study, we improve the calibration of the data using the data points of MASCS in 2007 and STIS in 2011 as a reference to fit VMC values (Table 1). To limit uncertainties that may arise from the influence of the aerosol scattering along the phase angle (α), we utilize only VMC data obtained at the same phase angle as either the MASCS ($\alpha = 85^\circ\text{--}90^\circ$) or STIS ($\alpha = 75^\circ\text{--}90^\circ$) observations. There are differences of 13 and 31 days from the closest VMC image at the time of the MASCS and STIS observations, respectively, at corresponding phase angles. To compensate for possible short-term fluctuations that may have occurred during those time periods, we derive the 80 days mean albedo observed by VMC in the low-latitude bin at the two phase angle bins of MASCS and STIS. We then use the 80 days mean albedo to calculate ratios of $A(\text{MASCS})/A(\text{VMC})$ at $\alpha = 85^\circ\text{--}90^\circ$ and $A(\text{STIS})/A(\text{VMC})$ at $\alpha = 75^\circ\text{--}80^\circ$, where A is the mean low-latitude albedo. Using this process, the ratios of 0.74 for $A(\text{MASCS})/A(\text{VMC})$ and 0.84 for $A(\text{STIS})/A(\text{VMC})$ were inferred. Differences in the ratios may result from differences in the latitudinal coverage of the MASCS and STIS observations (Figure 1) and may also incorporate a possible temporal variation of the sensitivity of VMC. Even though the latter is possible, the decreasing trend of low-latitude albedo between 2007 and 2011 changes from 29% to 24% in the low-latitude polynomial fit (Figure 5), which is yet a minor effect on the results of this study. Using the mean value of the ratios, 0.79, over all of the VMC data, the VMC and UVI albedo retrievals become reasonably comparable (Figure 5). Thus, we adopt this value and apply a new modified VMC calibration correction factor of 1.58 ($\beta = 2.0 \times 0.79$) to the VMC data used in our study. As Figure 5 shows, when the modified calibration correction factor is applied, the 365 nm albedo observed by VMC and UVI are reasonably aligned; those in 2008–2009 (VMC) are overlapped data in 2016 (UVI).

3.2. Whole-disk Albedo

In order to evaluate the robustness of the 1.58 modified VMC calibration correction factor, we employ 82 images taken with UVI in 2011 to compare with VMC. These UVI images

were obtained after the first failure of the planned Venus orbit insertion of *Akatsuki* (Nakamura et al. 2014). In those images, the apparent size of Venus is a few pixels across, but sufficient signal-to-noise ratios were achieved. We calculated the whole-disk albedo, $A_{\text{whole-disk}}$, which is a function of phase angle (α), following the equation (Sromovsky et al. 2001)

$$A_{\text{whole-disk}}(\alpha) = \frac{\pi}{\Omega_{\text{Venus}}} \frac{d_{\text{Venus}}^2 F_{\text{Venus}}}{S_{\odot}}, \quad (9)$$

where d_{Venus} is the Venus distance to the Sun (au), F_{Venus} is the measured disk-integrated Venus flux ($\text{W m}^{-2} \mu\text{m}^{-1}$), Ω_{Venus} is the solid angle of Venus as seen from the spacecraft (sr), and S_{\odot} is the solar irradiance at 1 au ($\text{W m}^{-2} \mu\text{m}^{-1}$), which is calculated for either UVI or VMC, using each of the transmittance functions.

The observed solid angle of Venus, Ω_{Venus} , is calculated as

$$\Omega_{\text{Venus}} = \pi \left(\sin^{-1} \left(\frac{r_{\text{Venus}}}{d_{\text{V-sc}}} \right) \right)^2, \quad (10)$$

where r_{Venus} is the cloud-top level radius of Venus (6052 + 70 km), and $d_{\text{V-sc}}$ is the distance of the spacecraft from Venus (km). The observed Venus flux, F_{Venus} , is calculated as

$$F_{\text{Venus}} = \sum_{r < r_o} R_{\text{obs}}(x, y) \times \Omega_{\text{pix}}, \quad (11)$$

where (x, y) is a location of a pixel in the image, Ω_{pix} is a solid angle of 1 pixel of either VMC or UVI, R_{obs} is the radiance ($\text{W m}^{-2} \text{sr}^{-1} \mu\text{m}^{-1}$) in the target area ($r < r_o$), and r is the distance of (x, y) from the Venus disk center (emission angle 0°). Here r_o is the radius range in which the measured radiances are summed, considering the point-spread function of the instrument (5 pixels) that is the required radius of the aperture photometry of the UVI star flux analysis. The whole-disk albedo can be expressed as $A_g \Phi(\alpha)$, where A_g is the geometric albedo, and $\Phi(\alpha)$ is the phase law of Venus, describing the disk-integrated

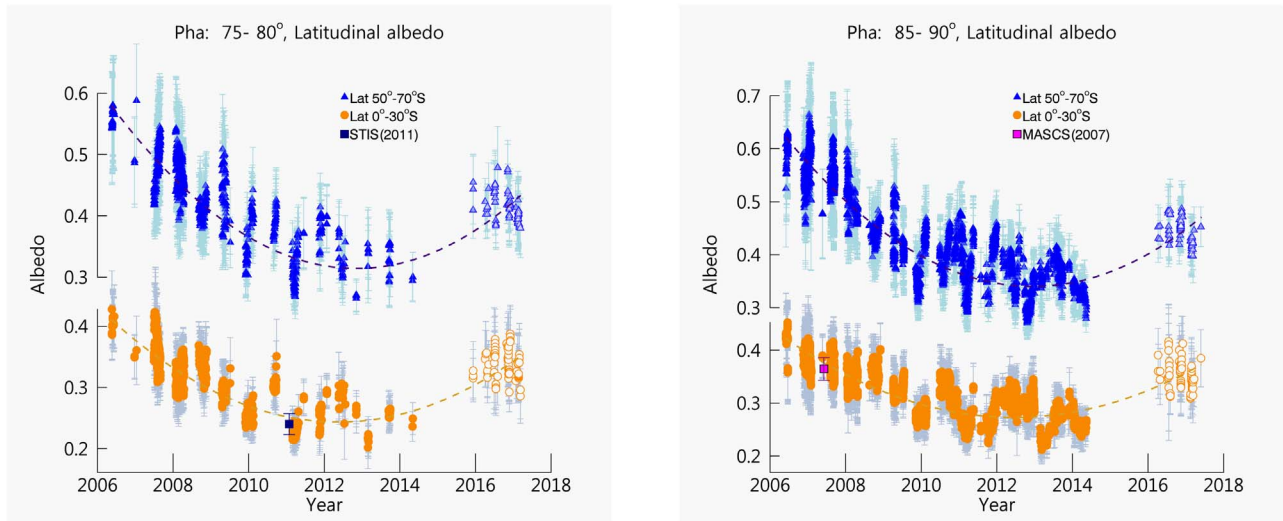


Figure 5. Long-term variations of the 365 nm albedo from 2006 to 2017 based on VMC (filled symbols), UVI (open symbols), STIS (navy square), and MASCS (magenta square). The low- (0–30°S) and high- (50–70°S) latitudinal mean albedo observed at the 75°–80° and 85°–90° phase angles are shown in the left and right panels, respectively. A polynomial fit of temporal variation in the derived latitudinal mean albedo (dashed lines) highlights the overall temporal trend. Error bars are standard deviations of albedo.

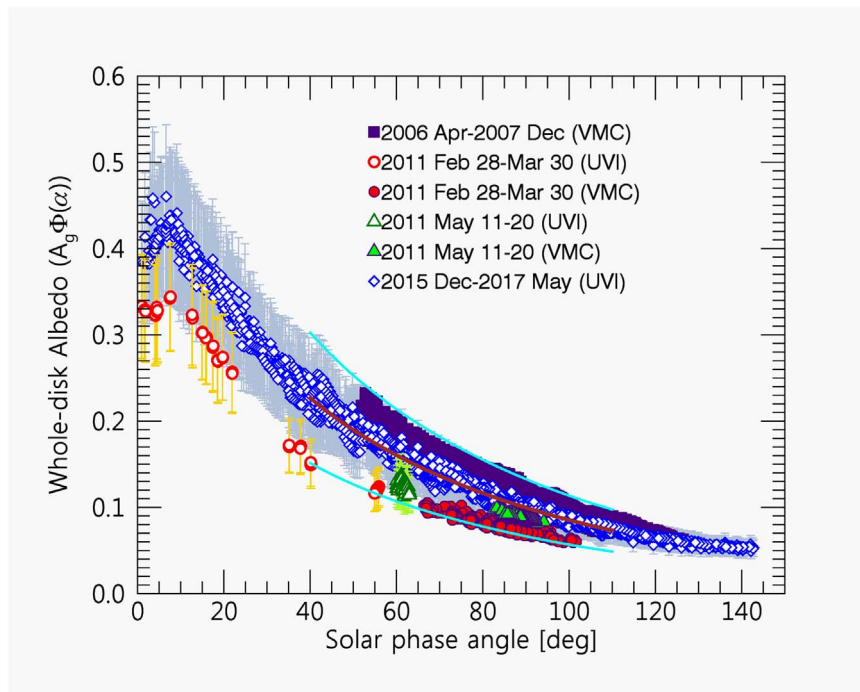


Figure 6. Whole-disk albedo observed over a range of phase angles by VMC in 2006–2007 and 2011 and by UVI in 2011 and 2015–2017. The error bar of UVI is the measurement error. The solid brown line is the polynomial fit to the 2015 December–2017 May UVI data observed at phase angles of 40°–110°; the solid cyan lines highlight temporal albedo variations from 2006–2007 (upper line) to 2011 (lower line), where the relative shape of the phase angle dependence is assumed constant. The lower cyan line demonstrates successfully that UVI and VMC data in 2011 February–March are aligned on one phase curve.

scattering efficiency as a function of phase angle (García Muñoz et al. 2014, 2017).

3.2.1. Comparison of the Whole-disk Albedo of VMC and UVI

We calculated the whole-disk albedo, $A_{\text{whole-disk}}$ (Equation (9)), of the 82 UVI images in 2011 and all of the disk-resolved VMC and UVI images. The latter is possible because our analysis is restricted to the images for which the observable dayside, defined by the observation elongation

angle, is fully captured within the field of view of the cameras (see Figure 2). The 1.58 modified calibration correction factor is applied to the VMC data.

Figure 6 shows the results of the whole-disk albedo versus phase angle. The 82 UVI images taken in February–March (circles) and May 11–20 (triangles) are compared to the VMC images obtained contemporaneously. As a reference, the whole-disk albedo results derived from 2015–2017 UVI data and 2006–2007 VMC data are also included in the plot. The vertical bar of UVI data indicates the 18% error in the absolute

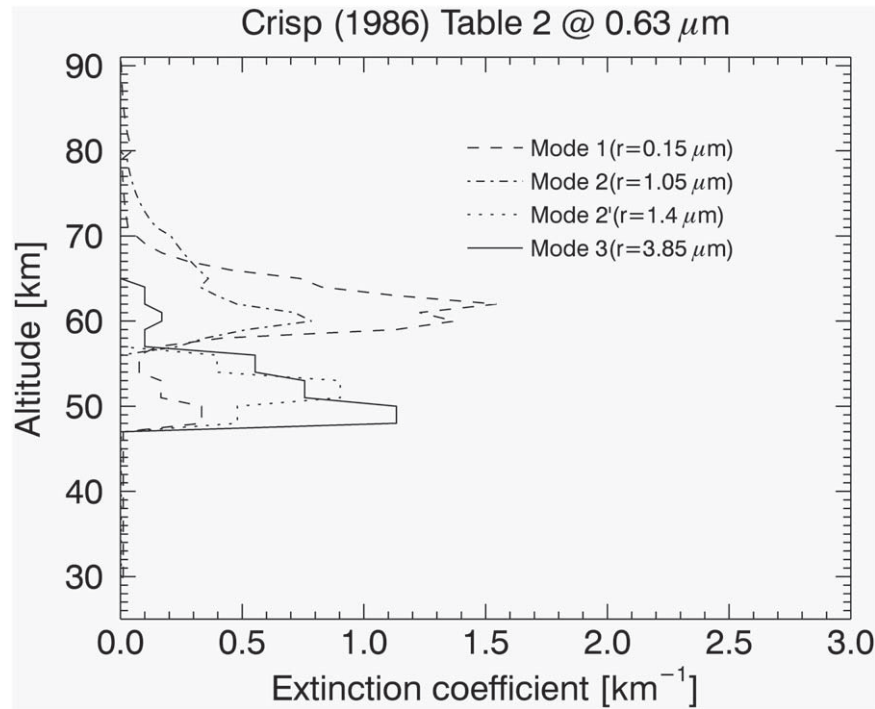


Figure 7. Vertical profile of the cloud extinction coefficient used in this study.

radiance (Section 2). The fractions of the disk illuminated by the Sun change with the solar phase angle, from 100% at 0° phase angle to 0% at 180° phase angle, so there is a dominant decreasing trend as the phase angle increases. At small phase angles, a local minimum related to glory is apparent (García Muñoz et al. 2014; Lee et al. 2017). The polynomial fit of UVI’s 2015–2017 data shows the empirical phase function $\Phi(\alpha)$ in the 40° – 110° phase-angle range (brown solid line; the equation is shown in Table 2). We shift this phase function vertically to fit the maximum and minimum VMC whole-disk albedo at a 75° – 80° phase angle (cyan lines), assuming a change of geometric albedo A_g over time, whereas the scattering properties Φ are the same. The lower cyan line that fits the VMC whole-disk albedo in 2011 February–March encompasses the UVI data at the same period. This means that the 1.58 modified calibration correction factor for VMC data works well.

In addition, our analysis of the 2011 and 2015–2017 UVI whole-disk albedo at 0° phase angle, which is a geometric albedo A_g , increases from ~ 0.33 in 2011 to ~ 0.40 in 2015–2017. This result confirms the increasing albedo trends from 2011 to 2015–2017 observed at high and low latitudes based on the recalibrated disk-resolved 2011 VMC and disk-resolved 2015–2017 UVI data (Figure 5). The observation of an increasing albedo over these time periods completely opposes the behavior that would be produced by progressive long-term UV sensor degradation (Shalygina et al. 2015). This cannot be used to investigate the influence of surface topography on the 365 nm albedo because for each date, a broad range of longitudes is included in the derivation of the albedo at small phase angles; this includes the 150 – 315°E range in 2011 March, 180 – 330°E in 2016 May, and 165 – (360) – 45°E in 2016 December–2017 January. Additionally, the 2011 UV data have insufficient spatial resolution to segregate specific longitude and latitude topographic regions.

Table 2
Coefficients of a Polynomial Fit, $y(\alpha) = \sum_{i=0}^n c_i \alpha^i$, Where $n \leq 8$, in Figures 6 and 8

	$\bar{A}_{\text{UVI,low-lat}}(\alpha)$	$\bar{A}_{\text{UVI,high-lat}}(\alpha)$	$\bar{A}_{\text{UVI,whole-disk}}(\alpha)$
c_0	0.18708465	0.47673713	0.62539023
c_1	0.0086404233	0.0029037657	-0.022833883
c_2	-0.00017491717	-0.00012465654	0.00063482472
c_3	1.1079428×10^{-6}	9.7921542×10^{-7}	$-1.2777032 \times 10^{-5}$
c_4			1.7206082×10^{-7}
c_5			$-1.4916523 \times 10^{-9}$
c_6			$7.9181817 \times 10^{-12}$
c_7			$-2.3230007 \times 10^{-14}$
c_8			$2.8698482 \times 10^{-17}$

3.3. Radiative Transfer Model

We use a one-dimensional line-by-line radiative transfer model (SHDOM; Evans 1998, 1998) in the 0–100 km altitude range and the 2000 – $50,000 \text{ cm}^{-1}$ ($=0.2$ – $5 \mu\text{m}$) range to estimate the abundance of the unknown absorber that fits the observed 365 nm albedo and to calculate the solar heating rate at low latitudes at the local noon time. The configurations are the same as those used in Lee et al. (2015b, 2016). The CO_2 line parameters were taken from a combined HITEMP2010 (Rothman et al. 2010) and one developed by Wattson & Rothman (1992) and Pollack et al. (1993), as described in Lee et al. (2016). We included collision-induced CO_2 absorption in the near-infrared and that of H_2O (Lee et al. 2016). Line parameters of other gases, N_2 , SO_2 , OCS , HCl , CO , HF , and H_2S , were taken from HITRAN2012 (Rothman et al. 2013), and vertical profiles of gaseous abundances were taken from Titov et al. (2007). We included Rayleigh scattering (Pollack 1967; Hansen & Travis 1974) and UV-range absorption cross sections of SO_2 (Wu et al. 2000). The microphysical properties of the cloud aerosols (modes 1, 2, 2’,

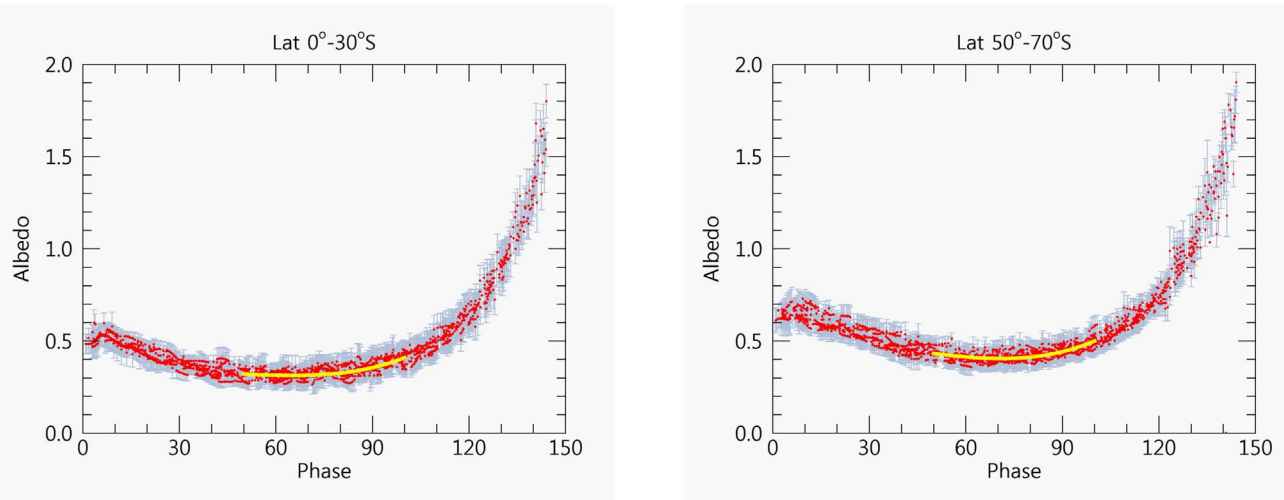


Figure 8. Phase curve of mean A at low (left) and high (right) latitudes in 2016–2017. Yellow lines are empirical polynomial fits. Vertical bars are standard deviations.

and 3) were taken from Zasova et al. (2007). We took the vertical structures of the clouds’ extinction coefficient from Crisp (1986), as shown in Figure 7. For the unknown absorber, we assumed Crisp’s (1986) absorption coefficient (Q_{abs}) of the mode 1 particle ($0.15 \mu\text{m}$ mean radius cloud particles; Kawabata et al. 1980; Knollenberg & Hunten 1980; Wilquet et al. 2009; Luginin et al. 2016) in the $0.3\text{--}0.8 \mu\text{m}$ spectral range in the upper cloud layer ($57\text{--}71 \text{ km}$). This assumed vertical location of the unknown absorber has been widely adopted in previous solar heating calculations (Crisp 1986; Lee et al. 2015b; Haus et al. 2016).

4. Results

4.1. Temporal Variations of Low- and High-latitudinal Albedo

The albedo A (Equation (9)) is phase angle α dependent due to strong backward and forward aerosol scatterings (García Muñoz et al. 2014; Lee et al. 2015a; Shalygina et al. 2015). Therefore, we restrict a comparison of $A(\alpha)$ to data obtained at near-equivalent phase angle bins. Figure 5 shows the temporal evolution of Venus’s low- and high-latitudinal mean albedo obtained at phase angles of $75^\circ\text{--}80^\circ$ and $85^\circ\text{--}90^\circ$. In this figure, a strong and steady decline in the albedo occurs between 2006 and 2011, from 0.4 to 0.25 at low latitudes and from 0.6 to 0.3 at high latitudes. Albedos at low and high latitudes in 2015 December–2017 May are restored to the 2008–2009 values.

While direct comparison of the mean A should be done using data at a specific phase angle bin, often there are missing data over time due to regular changes in phase angles along the orbit of the spacecraft. In order to have better temporal coverage of the mean A variations, we calculate the percent deviation of A from the 2016–2017 mean phase curve, $\bar{A}_{\text{UVI}}(\alpha)$, which is derived as a polynomial fit of UVI data in 2016–2017 in the $50^\circ\text{--}100^\circ$ phase angle range (Figure 8). Table 2 shows the coefficients of the polynomial fit to the mean phase curves at low and high latitudes. Deviations from the UVI phase curve are defined as

$$\text{Deviation (\%)} = \frac{A(\alpha) - \bar{A}_{\text{UVI}}(\alpha)}{\bar{A}_{\text{UVI}}(\alpha)} \times 100. \quad (12)$$

Figure 9 shows the percentage of deviations of mean A from $\bar{A}_{\text{UVI}}(\alpha)$ at low and high latitudes as a function of time, where phase angles from 50° to 110° are represented according to the

color bar at the top of each panel. The overall decline in the 365 nm albedo from 2006 to 2011 remains apparent. Additionally, relatively sharp albedo declines are observed at the ends of 2009 and 2010, and the beginning of 2013 that remain constant over short time periods (\sim months) before returning to the $\bar{A}_{\text{UVI}}(\alpha)$ level. The robustness of the darker albedo conditions observed at the beginning of 2011 is confirmed by the overlap with the 2011 January STIS data. At high latitudes, periods of albedo decrease are less pronounced and appear to be shorter-lived than those at low latitudes. This may be an indication of the combined influence of the unknown absorber abundance and the meridional circulation (Hadley circulation). In particular, the latter would remove older aerosols downward below the cloud-top level, following the descending branch at high latitudes (Imamura & Hashimoto 2001) and leaving behind only the bright, newly formed aerosols that support the existence of Venus’s bright high latitudes.

4.2. Temporal Variations of Whole-disk Albedo

We apply also Equation (12) for the whole-disk albedo $A_{\text{whole-disk}}$ and use the mean phase curve (Figure 6 and Table 2) to get the percent deviations of $A_{\text{whole-disk}}$ from the 2016–2017 mean phase curve. Figure 10 shows the result as a function of time. The same albedo decreases inferred from the disk-resolved data from 2006 to 2011 are shown in this whole-disk albedo analysis. The independent UVI data obtained in early 2011 (dots with error bars) are well overlapped with those of VMC, including the same short-term albedo variations between 2011 March and May. A darker 365 nm albedo in 2011 than in 2006–2007 or 2016–2017 is a common feature in both the disk-resolved latitudinal and disk-integrated data, implying that the 365 nm darkening that occurred between those dates was a global phenomenon.

4.3. Solar Heating Variations

Because of the influence of the unknown absorber on the solar heating rate near the cloud-top level (Crisp 1986; Titov et al. 2007; Lee et al. 2015b) owing to the broad absorption spectrum from UV to visible (Crisp 1986; Pérez-Hoyos et al. 2018), the long-term 365 nm albedo variation we present here should have had a significant effect on Venus’s solar heating

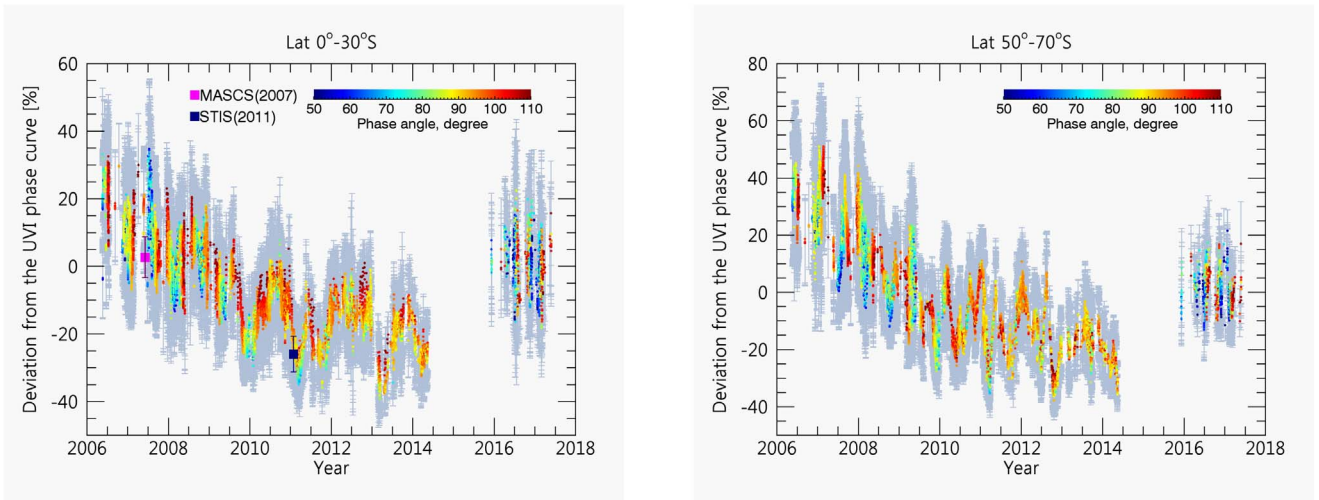


Figure 9. Relative temporal variations of mean A compared to the 2016–2017 phase curve, defined as Equation (12), at low (left) and high (right) latitudes. Vertical bars are standard deviations of mean A . The colors of the dots indicate phase angles between 50° and 110° , shown in the color bar. MASCS (2007) and STIS (2011) at low latitudes are shown with square symbols.

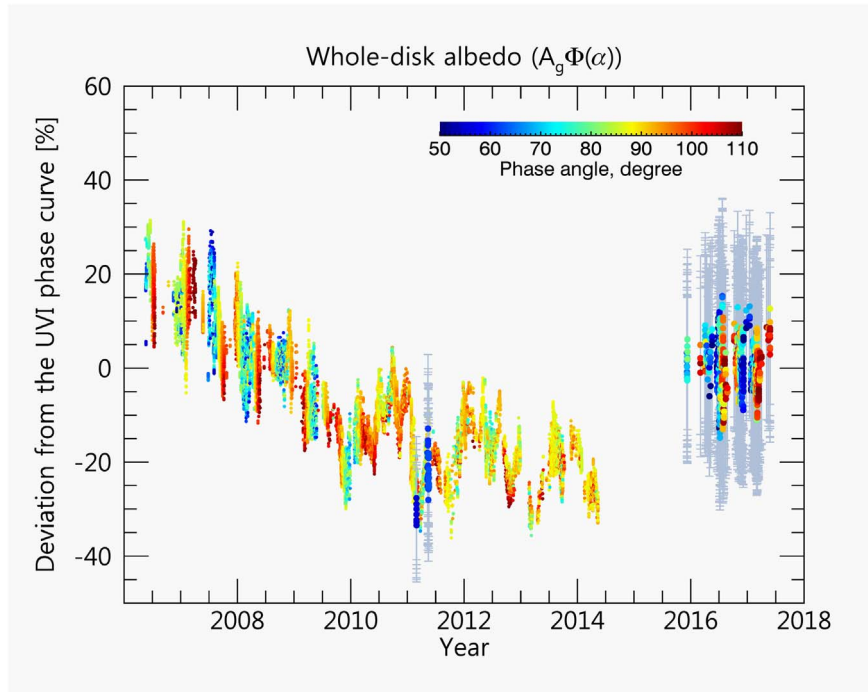


Figure 10. Deviations of the whole-disk albedo, $A_{\text{whole-disk}}$, of all VMC (2006–2014) and UVI (2011, 2015–2017) data. Vertical bars of UVI correspond to the 18% error in the absolute radiance inferred from the star calibration. The symbol colors indicate the phase angle, as defined in the color bar.

rate. We use the radiative transfer model (Section 3.3) to determine a required abundance of the unknown absorber, which is assumed to be fixed to the mode 1 particles in the 57–71 km altitude range (Section 3.3), and to estimate the resulting solar heating rate changes at low latitudes. We incorporate the observed low-latitudinal 365 nm albedo variations into our model using a scaling factor f that is multiplied by the assumed initial absorption coefficient Q_{abs} taken from Crisp (1986) for the unknown absorber. Here $f = 1.0$ means the initial value, and $f > 1.0$ means the more abundant unknown absorber, which results in a darker albedo, and

vice versa. So we control only the single scattering albedo of the mode 1 particles, but not the size of the particles. In order to fit the observed A , we calculate five sets of emission (e) and incident (i) angles that satisfy $\alpha = 88^\circ$ —(e, i) = ($28^\circ, 60^\circ$), ($38^\circ, 50^\circ$), ($48^\circ, 40^\circ$), ($58^\circ, 30^\circ$), and ($68^\circ, 20^\circ$)—to simulate different combinations of e and i . The resulting radiance factors are corrected using the same photometric law that was applied to the calculation of the albedo (Section 3.1.2), and the mean value is used to find f values that match the observed albedo.

Figure 11 shows the relationship of f and the mean value of the calculated 365 nm albedo for the 88° phase angle

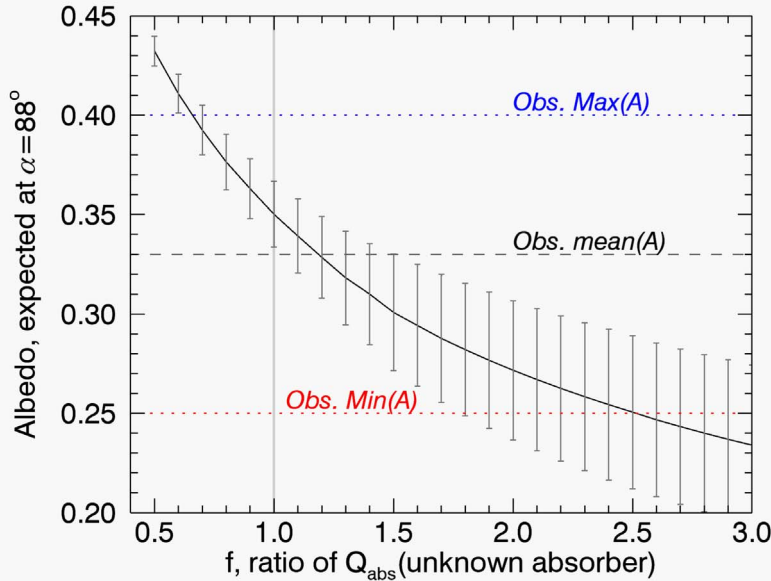


Figure 11. Expected albedo as a function of f . Vertical error bars correspond to uncertainties depending on incidence and emission angles (see text for details).

conditions (Figure 5). The mean albedo observed at low latitudes is 0.33 and requires $f = 1.18$. This is close to the initial value, $f = 1.0$, that results in a calculated albedo, $(A) = 0.35$. The approximate maximum albedo observed at low latitudes, $A = 0.40$, requires $f = 0.65$, and the minimum albedo, $A = 0.25$, requires $f = 2.51$. We employ these f values in net solar flux profile calculations at 15° latitude, which is the middle of the low-latitude bin, at local noon time. Figure 12 shows the net solar flux divergence spectrum as a function of altitude z , $-\nabla \cdot F_{\text{net}} = -(dF_{\text{net}}/dz)$, where F_{net} is the net solar flux. The strongest influence of the unknown absorber appears around 400 nm, where decreasing absorption and increasing solar irradiance overlap.

Figure 13 shows the calculated local noon time solar heating rate at 15° latitude, derived from Figure 12. This represents that the solar heating rate varied from -25% to $+40\%$ from the mean (2006–2017), which is a significantly large range. The peak of the solar heating rate is $36 \text{ K (Earth) day}^{-1}$ for the mean albedo condition, 49 K day^{-1} for the minimum albedo, and 27 K day^{-1} for the maximum albedo at this local noon time.

We note that the vertical structure of the upper clouds may affect the solar heating rate (Lee et al. 2015b), but the structure of the upper clouds at low latitudes from near-infrared observations is shown to be rather stable during the time of *Venus Express* (Ignatiev et al. 2009; Cottini et al. 2015; Fedorova et al. 2016), validating the use of a fixed cloud structure. Other analyses suggest that the vertical distribution of the unknown absorber may sometimes extend vertically above the cloud-top level (Molaverdikhani et al. 2012; Lee et al. 2015a). However, the upper haze and vertical locations of the unknown absorber are not changed in our calculations, as these are beyond the scope of this study. Further sensitivity studies on solar heating rate would explore in depth the effects of variable vertical and latitudinal distributions of the unknown absorber on Venus’s global solar heating rate.

5. Discussion

5.1. Relationship between Solar Heating and Zonal Winds at the Cloud-top Level

The observed 365 nm albedo variations should result in solar heating variations near the cloud-top level as shown in Section 4.3. We note that two long-term trends occurred in parallel. In the period when the 365 nm albedo had declined, leading to increases in solar heating, the long-term cloud-top zonal wind was observed to increase from $80\text{--}90$ to $\sim 110 \text{ m s}^{-1}$ between 2007 and 2012 around local noon at 20°S (Khatuntsev et al. 2013; Kouyama et al. 2013; Hueso et al. 2015). Likewise, between 2014 and 2016, when the 365 nm albedo had increased, leading to decreases in solar heating, the zonal wind speed was observed to slow down from 110 to 100 m s^{-1} (Horinouchi et al. 2018). This wind speed variation is qualitatively consistent with the expected change in vertical shear associated with cyclostrophic balance. As the strongest solar heating occurs at low latitudes, the low-latitude heating can alter the pole-to-equator gradient of temperature. The increased low-latitude solar heating inferred from the 2011 to 2013 period should have increased the meridional temperature gradient, which then increases the equilibrium vertical shear, leading to an increase of wind speed. Additionally, there would be contributions of change of momentum flux associated with the thermal tide, which has been expected to participate in the angular momentum budget. To test these ideas, a simulation was run with the latest version of the Institut Pierre Simon Laplace (IPSL) Venus Global Climate Model (GCM; Garate-Lopez & Lebonnois 2018). Starting from the reference simulation (see the Appendix for details), the solar heating rate was modified as a function of time, slowly reducing it (the whole profile at the same time, a simple test adjustment) over 20 Venusian solar days, i.e., 2340 Earth days or 6.4 Earth yr. The rate of solar heating change is -40% in 6.4 yr (from 7.5 to 4.5 K day^{-1} in zonal mean solar

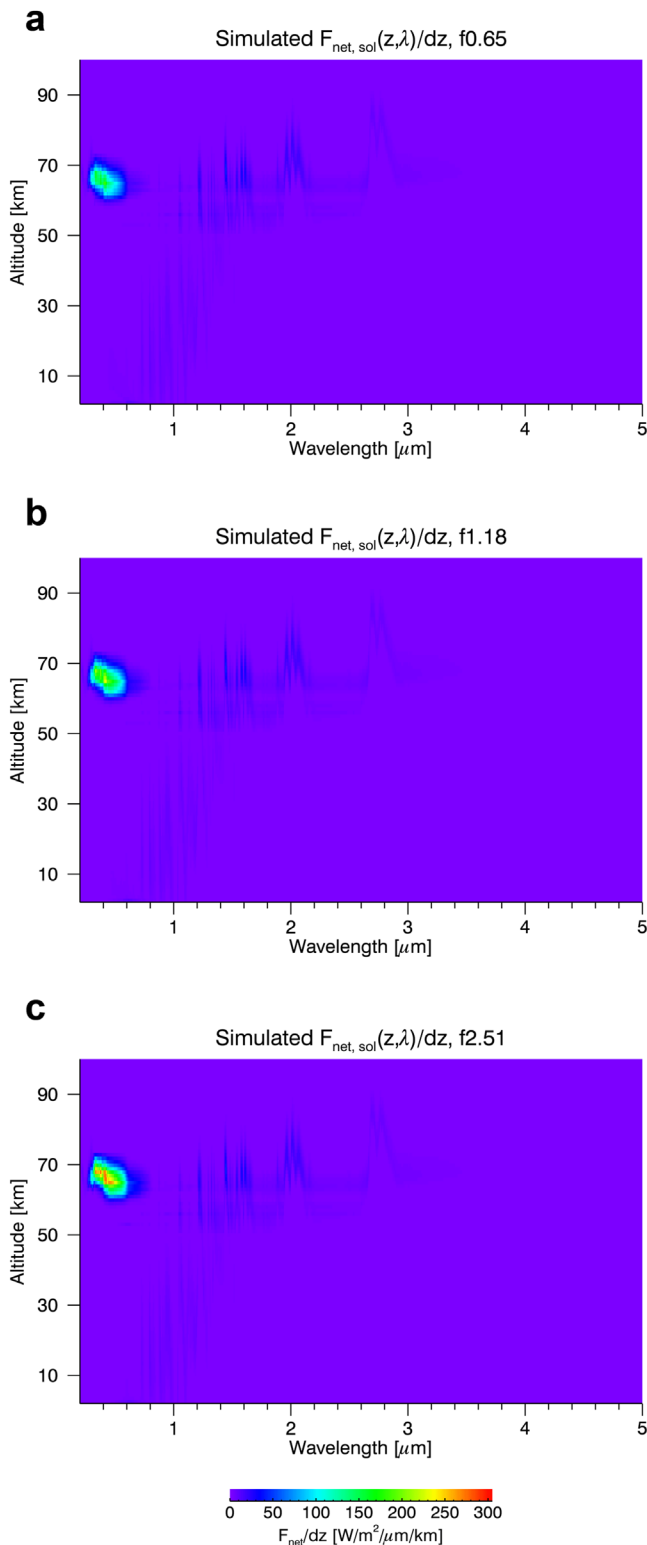


Figure 12. Net solar flux divergence as functions of wavelength and altitude at local noon time at 15°S . Here (a) $f = 0.65$, (b) $f = 1.18$, and (c) $f = 2.51$ are multiplied by the extinction coefficients of the unknown absorber (Q_{abs}) in the 57–71 km altitude range and the 0.3–0.8 μm range (see text for details). Spectral features are smoothed over a 0.01 μm interval.

heating rate), consistent with the evolution proposed in this study. The time evolution of the zonally averaged solar heating rate in the latitudinal band between 10°S and 20°S and at 30 mbar (~ 70 km, near the cloud-top level) is plotted in

Figure 14, together with the simultaneous evolution of the temperature and zonal wind in the same region. There is a clear correlation between these variables with an amplitude only slightly higher than the observed zonal wind variations. This correlation is caused by a reduced meridional circulation that directly affects the transport of angular momentum upward and poleward, resulting in a reduction of the cloud-top zonal wind peak. A detailed analysis is given in the Appendix.

5.2. Possible Causes of the Observed Albedo Variations

There are many intervening agents that may act in combination to produce the observed albedo variations, for example, the chemical composition and reaction rate of the unknown absorber, its interaction with or dependency on the chemical state of other atmospheric constituents, and the variability of the cloud and haze structure as a function of time. We note that the SO_2 abundance above the cloud-top level was observed to decline from 2007 to 2012 (Marcq et al. 2013) and then subsequently increase around 2016 (Encrenaz et al. 2019). Since the 365 nm albedo will become relatively brighter with more abundant pure sulfuric acid aerosols that are formed through photolysis of SO_2 , it is plausible that the observed albedo trend is linked to the long-term trend of SO_2 abundance.

The period of low 365 nm albedo in this study overlaps the known maximum time of the solar activity cycle (Jiang et al. 2018), as shown in Figure 15. This resembles the correlation of Neptune’s reflectivity and the solar activity cycle (Aplin & Harrison 2016). Since solar EUV radiation might affect photochemical reactions involving SO_2 that are necessary for aerosol formation on Venus (Mills et al. 2007; Parkinson et al. 2015), further study is required to explore the influence of the solar activity cycle on the Venusian atmosphere. It is also possible that the production rate of sulfuric acid aerosols is altered by galactic cosmic rays via ion-induced nucleation. Electrostatic interactions between ionized acid molecules can enhance new aerosol formation by reducing the critical size and increasing the collision possibility (Lovejoy et al. 2004; Kirkby 2007), and there are observations of $\text{H}_2\text{SO}_4\text{--H}_2\text{O}$ ultrafine aerosols of less than 9 nm in diameter in Earth’s upper troposphere and stratosphere that were explained by the ion-induced nucleation (Lee et al. 2003). The peak of the ion production rate in the Venusian atmosphere due to galactic cosmic rays is predicted at 62.5 km (Nordheim et al. 2015) with the 46–58 ion pairs $\text{cm}^{-3} \text{s}^{-1}$ range of variations between solar minimum and maximum. So, the upper haze aerosol formation might be effectively triggered by such ion-induced nucleation and vary following the solar activity. Figure 15 shows comparisons of the 365 nm albedo at low latitudes, neutron cosmic rays detected from the Oulu station,¹⁸ and Ly- α flux at the Earth location.¹⁹ A 5 day mean is applied to compare the 365 nm albedo and cosmic rays to compensate for the atmospheric rotation rate on Venus. The solar rotation rate (25 days) mean is applied for the comparison of the 365 nm albedo and Ly- α flux to take into account the different locations of Venus and the Earth with respect to the Sun. The results show that the 365 nm albedo A has a negative correlation with Ly- α flux and a positive correlation with neutron cosmic rays, but these may act together with the mesospheric SO_2 gas influences.

¹⁸ <http://cosmicrays oulu.fi>

¹⁹ http://lasp.colorado.edu/lisird/data/composite_lyman_alpha/

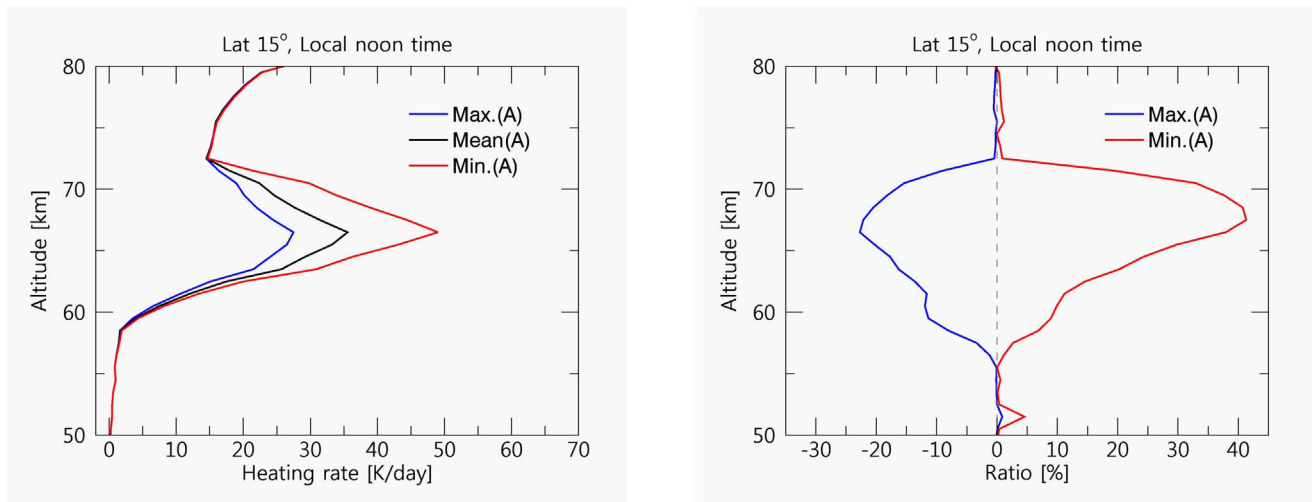


Figure 13. Calculated solar heating rate profiles for the observed maximum, minimum, and mean albedo at local noon time at 15°S . The solar heating rate is displayed in K day^{-1} (left) and as a relative ratio from the mean albedo (right).

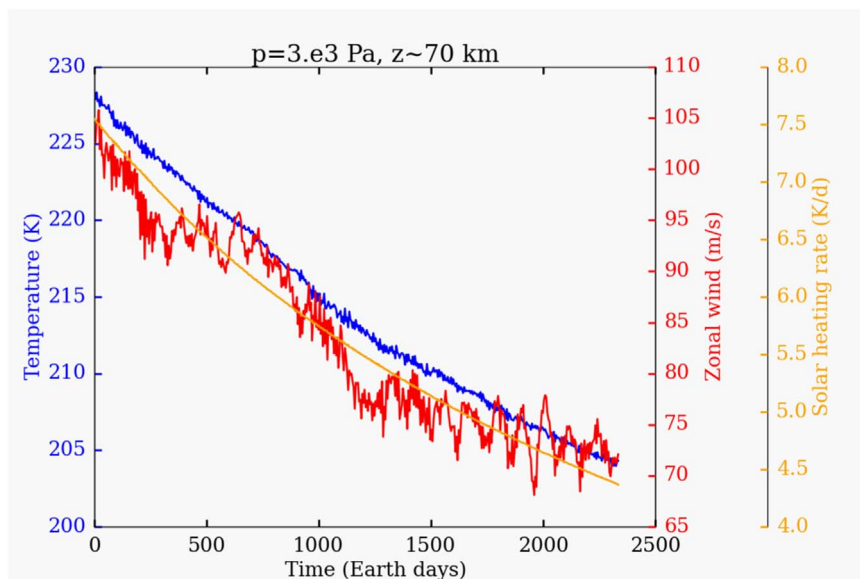


Figure 14. Temporal variations of zonal mean solar heating rate (orange), wind speed (red), and temperature (blue) at 10°S – 20°S at 30 mbar (~ 70 km). The solar heating rate is controlled to decrease smoothly along time by 40% from the reference condition in the IPSL Venus GCM (Appendix). Simultaneous variations in temperature and zonal wind speed are shown together.

5.3. Comparison with Other Planets

Regardless of the cause of the observed albedo changes, the range of albedo variation on Venus is surprising. On the Earth, clouds play a considerable role as a buffer of possible climate variations and are also a regulator of the solar energy distribution (Stephens et al. 2015). However, the clouds on Venus are different; rather than supporting a stable solar heating rate, drastic variations of solar heating seem to occur as inferred from the 365 nm albedo. The astounding nature of the albedo variation results we present here is further emphasized by results derived from other planetary albedo studies in the solar system, where weaker long-term albedo variations were observed. For example, at Neptune, the observed magnitude varied by ± 0.02 (corresponding to $\pm 2\%$ changes in flux) at the blue (472 ± 10 nm) and red (551 ± 10 nm) filters over 1972–2014 (Aplin & Harrison 2016), and at Mars, the surface

albedo varied by 10% at the red filters (575–675 and 550–700 nm) from 1976–1980 to 1999–2003 (Geissler 2005).

5.4. Further Studies

In addition to the impact of the solar heating rates at the cloud-top level, the vertical profile of solar flux on Venus, down to the surface, should also be altered by the observed cloud-top albedo changes. Such solar flux variations may explain the unbalanced net radiative energy below the clouds (Lee et al. 2017); therefore, further investigation is needed to understand the true impact of the albedo changes on the entire lower atmosphere of Venus.

Our study focuses on the observed 365 nm albedo and its direct impacts on solar heating at the equator. This does not cover detailed modeling of net radiative forcing, such as cooling rate changes (Haus et al. 2017), that would impact the

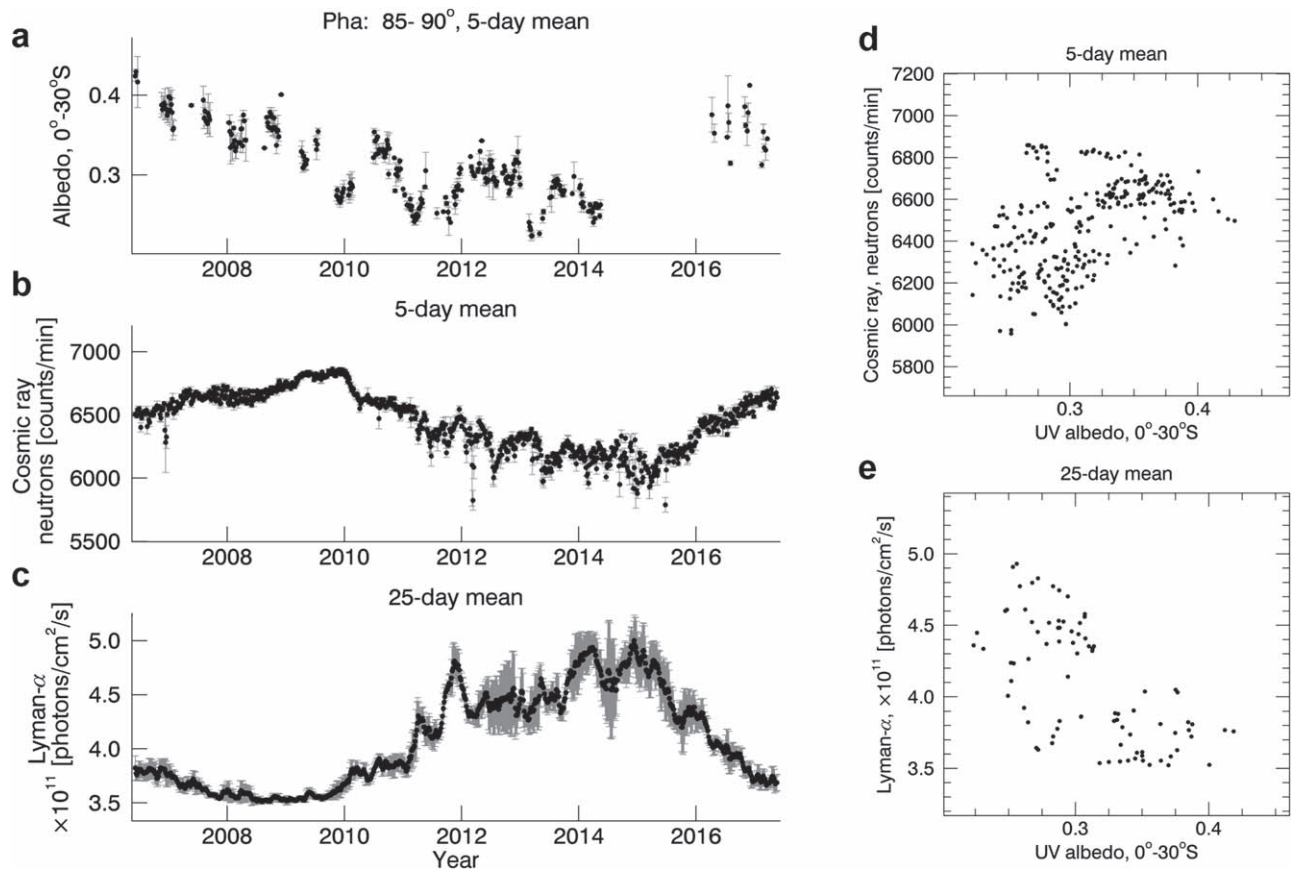


Figure 15. Comparison of the 365 nm albedo A , neutron cosmic rays, and Ly- α flux density evolution with time. On each date, the 5 day mean of low-latitude A at the 85°–90° phase angle bin (a), the 5 day mean of cosmic rays (neutron) measured at the Oulu station (b), and the 25 day mean of the Ly- α flux (c) is shown. A comparison between (a) and (b) is shown in (d). A comparison between (a) and (c) is shown in (e) but uses the 25 day mean for consistency. See text for details.

microphysical and photochemical processes. Such studies must be completed to accurately infer the true impact of the solar heating on cloud formation and climate. The work we present here provides a foundation for future in-depth studies of links between Venus’s 365 nm albedo and the processes that directly impact Venus’s climate.

6. Summary

We present the intense decadal variation of Venus’s 365 nm albedo between 2006 and 2017; the maximum albedo occurred in 2006–2007, the minimum in 2011–2014, and the recovery of albedo in 2016–2017 to the level in 2008–2009. This trend is consistent among four independent UV instruments, VMC and MASCS in 2007 and VMC, STIS, and UVI in 2011, using either disk-resolved or disk-integrated data. We discard the previously suggested sensitivity degradation of VMC (Shalygina et al. 2015) and propose a new calibration correction factor for VMC in this study. The ranges of albedo variations are ~ 0.2 – 0.4 at low latitudes and ~ 0.3 – 0.6 at high latitudes in 2006–2017, so albedo has varied by a factor of 2 over the last decade. The whole-disk albedo also shows a similar trend, changed from -30% to $+20\%$ compared to the mean value in 2016–2017, meaning that the albedo variation occurred on a global scale.

Our one-dimensional line-by-line radiative transfer model calculations reveal that this level of albedo variation can alter the solar heating rate from -25% to $+40\%$ due to the broad absorption spectrum of the unknown absorber from the UV to visible range.

We suggest that this solar heating rate variation can be a cause of the observed long-term zonal wind speed variation at low latitudes that increased from 80 – 90 m s^{-1} in 2007 to ~ 110 m s^{-1} in 2012 and then decreased to 100 m s^{-1} in 2016–2017. Wind speed increased during the low-albedo time, when solar heating was stronger than average, implying that increased solar heating may play a role in wind speed changes through cyclostrophic balance, enhanced thermal tide, or vertical momentum transport. We show the results of Venus GCM simulations, which support the linear relationship between solar heating rate and zonal wind speed.

The observed 365 nm albedo variations might be caused by variations of SO_2 gas abundance above the clouds. We also suggest links between the 365 nm albedo and the solar cycle and consequent galactic cosmic-ray density variations. Continuous 365 nm observations are necessary to clarify the mechanism of the 365 nm albedo variations.

Y.J.L. thanks T. Satoh, R. Lorenz, N. Ignatiev, R. Hueso, and C.C.C. Tsang for helpful comments. K.-L.J. was supported by the NASA/PS program, grant NNX16AK82G, for the analysis of the 365 nm STIS data. S.P.-H. was supported by the Spanish MICIIN project AYA2015-65041-P (MINECO-FEDER, 695UE) and Grupos Gobierno Vasco IT-765-13. S.L. acknowledges support from INSU-PNP. The IPSL VGCM computations were done thanks to the High-Performance Computing (HPC) resources of the Centre Informatique National de l’Enseignement Supérieur (CINES) under allocation No. A0040110391 made by the Grand Équipement National de Calcul Intensif (GENCI). J.P. acknowledges the

JAXA's International Top Young Fellowship. Solar heating calculations were performed on a Supermicro SuperServer Intel (R) Xeon(R) CPU E5-2620 v4 funded through JAXA's International Top Young Fellowship. T.H., M.T., and T.I. acknowledge JSPS grant 16H02231. S.Li. was supported by a NASA Participating Scientist in Residence grant (NNX16AC79G). E.M. acknowledges support from CNES and INSU-PNP for SPICAV data analysis.

Appendix

Brief Description of the IPSL Venus GCM and Analysis of the Simulation Results

The IPSL Venus GCM has successfully demonstrated the development of strong zonal wind near the cloud-top level (Lebonnois et al. 2016). Upgrading the GCM (Garate-Lopez & Lebonnois 2018) employed latitudinally varying cloud structures (Haus et al. 2014). The authors also used a solar heating lookup table (Haus et al. 2015) according to the latitudinal cloud structures. Thermal cooling is based on the net exchange rate formalism (Eymet et al. 2009) with additional continua. This last version of the IPSL Venus GCM was able to simulate a prominent cold band surrounding the poles of Venus close to the observations (Garate-Lopez & Lebonnois 2018).

In this latest IPSL Venus GCM, only solar heating has been reduced, mimicking the expected solar heating rate variations shown in this manuscript. Figure 14 presents the linear correlation among solar heating, temperature, and zonal wind

speed. To interpret these correlations, the time variations of the latitudinal profiles of zonally and temporally (over 2 Venusian solar days) averaged heating rates (solar, infrared, and dynamical terms of the energy budget), temperature, and vertical and zonal winds are plotted in Figure 16 at 30 mbar.

Looking at the different heating rates (Figure 16(a)), it appears that, on average, the decrease of the solar heating is mostly compensated for by a decrease of the infrared cooling, corresponding to the decrease in temperature (Figure 16(b)). At mid- to high latitudes, though, the dynamical term associated with averaged meridional and vertical motions is not negligible; therefore, the decrease of the solar heating is compensated for by an impact on the averaged meridional and vertical winds. A reduction of the amplitude of the vertical wind is seen in Figure 16(c), except between 30° and 50° of latitude, which may indicate some impact here of changes in the meridional energy budget. This reduction of the mean meridional circulation has a direct impact on the transport of angular momentum upward and poleward, inducing a reduction of the cloud-top zonal wind peak (Figure 16(d)). Regardless of the simplicity of the simulation setup, the results explain how solar heating variations can affect zonal winds. It will be important to compare with long-term temperature trend analyses that may be available in the near future using the nightside temperature field retrieved from VIRTIS-H/*Venus Express* (Migliorini et al. 2012) or radio occultation temperature profiles from VeRa/*Venus Express* (Tellmann et al. 2012).

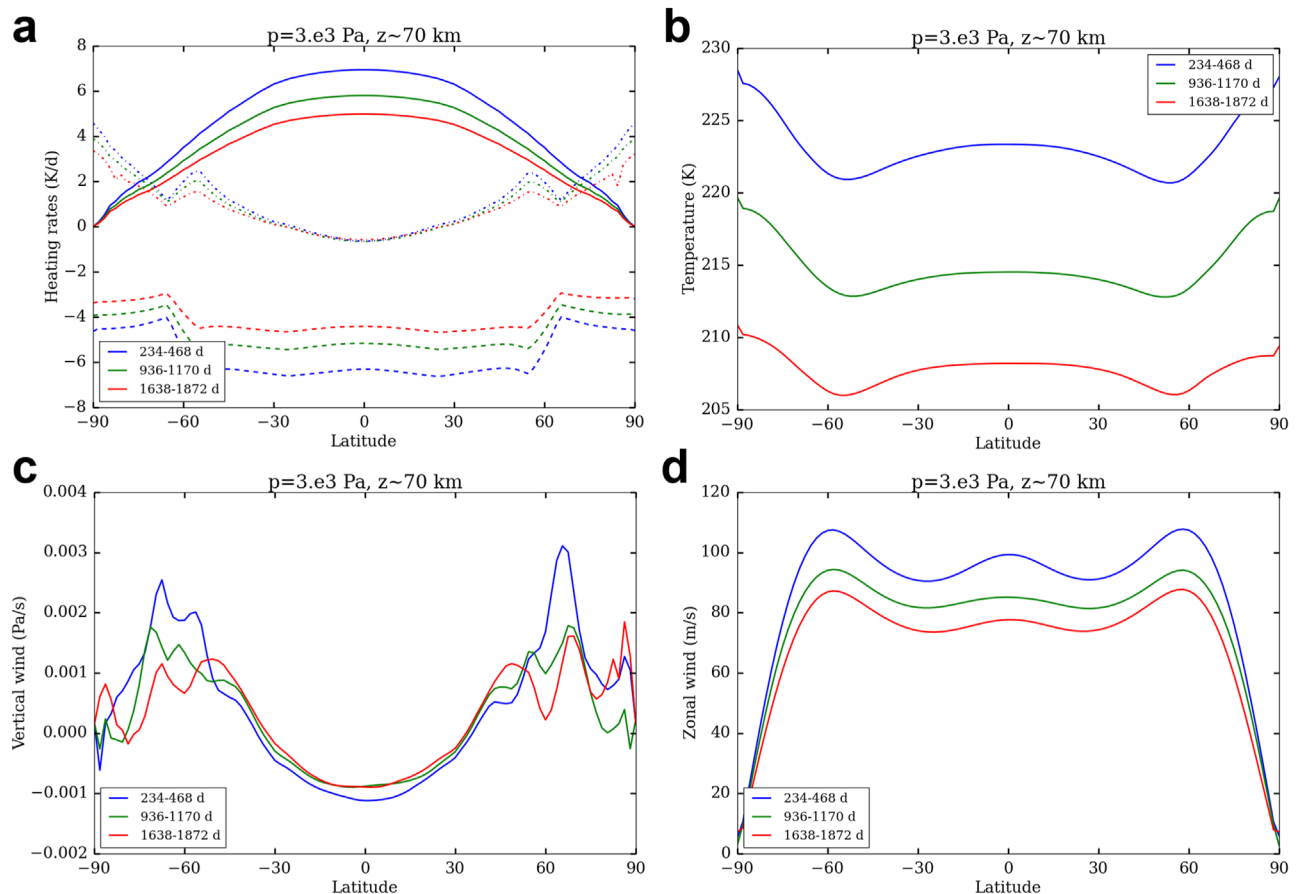














Figure 16. Latitudinal heating rate (a), temperature (b), vertical winds (c), and zonal winds (d) at 30 mbar (~ 70 km) in the same simulation shown in Figure 14. All parameters are averaged zonally over 2 Venusian solar days, as shown in the legend of each panel. In (a), solar heating (solid lines), thermal heating (dashed lines), and adiabatic heating (dotted lines) are compared, and negative values mean cooling.

ORCID iDs

Yeon Joo Lee  <https://orcid.org/0000-0002-4571-0669>
 Santiago Perez-Hoyos  <https://orcid.org/0000-0002-2578-4682>
 Dmitriy V. Titov  <https://orcid.org/0000-0001-7673-9061>
 Sebastien Lebonnois  <https://orcid.org/0000-0002-2390-8164>
 Javier Peralta  <https://orcid.org/0000-0002-6823-1695>
 Takeshi Horinouchi  <https://orcid.org/0000-0002-2296-1975>
 Takeshi Imamura  <https://orcid.org/0000-0002-9470-4492>
 Emmanuel Marcq  <https://orcid.org/0000-0002-1924-641X>
 Masahiro Takagi  <https://orcid.org/0000-0002-4629-6279>
 Manabu Yamada  <https://orcid.org/0000-0003-0726-6592>
 Shin-ya Murakami  <https://orcid.org/0000-0002-7137-4849>
 Kazunori Ogohara  <https://orcid.org/0000-0001-7666-4442>

References

- Allen, C. W. 1964, *Astrophysical Quantities* (2nd ed.; London: Athlone Press)
- Aplin, K. L., & Harrison, R. G. 2016, *NatCo*, **7**, 11976
- Barker, E. S., Woodman, J. H., Perry, M. A., Hapke, B. A., & Nelson, R. 1975, *JATs*, **32**, 1205
- Bertaux, J.-L., Khatuntsev, I. V., Hauchecorne, A., et al. 2016, *JGRE*, **121**, 1087
- Boyer, C., & Camichel, H. 1961, *AnAp*, **24**, 531
- Buratti, B., & Veverka, J. 1983, *Icar*, **55**, 93
- Chance, K., & Kurucz, R. L. 2010, *JQSRT*, **111**, 1289
- Cottini, V., Ignatiev, N. I., Piccioni, G., & Drossart, P. 2015, *P&SS*, **113**, 219
- Crisp, D. 1986, *Icar*, **67**, 484
- Del Genio, A. D., & Rossow, W. B. 1982, *Icar*, **51**, 391
- Del Genio, A. D., & Rossow, W. B. 1990, *JATs*, **47**, 293
- Encrenaz, T., Greathouse, T. K., Marcq, E., et al. 2019, *A&A*, **623**, A70
- Esposito, L. W. 1980, *JGRA*, **85**, 8151
- Esposito, L. W., & Travis, L. D. 1982, *Icar*, **51**, 374
- Evans, K. F. 1998, *JATs*, **55**, 429
- Eymet, V., Fournier, R., Dufresne, J. L., et al. 2009, *JGRE*, **114**, E11008
- Fedorova, A., Marcq, E., Luginin, M., et al. 2016, *Icar*, **275**, 143
- Frandsen, B. N., Wennberg, P. O., & Kjaergaard, H. G. 2016, *GeoRL*, **43**, 11146
- Garate-Lopez, I., & Lebonnois, S. 2018, *Icar*, **314**, 1
- García Muñoz, A., Lavvas, P., & West, R. A. 2017, *NatAs*, **1**, 0114
- García Muñoz, A., Pérez-Hoyos, S., & Sánchez-Lavega, A. 2014, *A&A*, **566**, L1
- Geissler, P. E. 2005, *JGRE*, **110**, E02001
- Hansen, J. E., & Travis, L. D. 1974, *SSRv*, **16**, 527
- Hapke, B. 2012, *Theory of Reflectance and Emittance Spectroscopy* (2nd ed.; Cambridge: Cambridge Univ. Press)
- Haus, R., Kappel, D., & Arnold, G. 2014, *Icar*, **232**, 232
- Haus, R., Kappel, D., & Arnold, G. 2015, *P&SS*, **117**, 262
- Haus, R., Kappel, D., & Arnold, G. 2017, *Icar*, **284**, 216
- Haus, R., Kappel, D., Tellmann, S., et al. 2016, *Icar*, **272**, 178
- Holsclaw, G. M., McClintock, W. E., Domingue, D. L., et al. 2010, *Icar*, **209**, 179
- Horinouchi, T., Kouyama, T., Lee, Y. J., et al. 2018, *EP&S*, **70**, 10
- Hueso, R., Peralta, J., Garate-Lopez, I., Bandos, T. V., & Sánchez-Lavega, A. 2015, *P&SS*, **113**, 78
- Hummel, J. R., Shettle, E. P., & Longtin, D. R. 1988, *A New Background Stratospheric Aerosol Model for Use in Atmospheric Radiation Models*, Technical Rept. ADA210110
- Ignatiev, N. I., Titov, D. V., Piccioni, G., et al. 2009, *JGRE*, **114**, E00B43
- Imai, M., Takahashi, Y., Watanabe, M., et al. 2016, *Icar*, **278**, 204
- Imamura, T., & Hashimoto, G. L. 2001, *JATs*, **58**, 3597
- Jessup, K. L., Marcq, E., Bertaux, J.-L., et al. 2019, *Icar*, **335**, 113372
- Jessup, K. L., Marcq, E., Mills, F., et al. 2015, *Icar*, **258**, 309
- Jiang, J., Wang, J.-X., Jiao, Q.-R., & Cao, J.-B. 2018, *ApJ*, **863**, 159
- Kawabata, K., Coffeen, D. L., Hansen, J. E., et al. 1980, *JGR*, **85**, 8129
- Khatuntsev, I. V., Patsaeva, M. V., Titov, D. V., et al. 2013, *Icar*, **226**, 140
- Kirkby, J. 2007, *SGeo*, **28**, 333
- Knollenberg, R. G., & Hunten, D. M. 1980, *JGR*, **85**, 8039
- Kouyama, T., Imamura, T., Nakamura, M., Satoh, T., & Futaana, Y. 2013, *JGRE*, **118**, 37
- Kouyama, T., Imamura, T., Nakamura, M., Satoh, T., & Futaana, Y. 2015, *Icar*, **248**, 560
- Krasnopolsky, V. A. 2017, *Icar*, **286**, 134
- Krasnopolsky, V. A. 2018, *Icar*, **299**, 294
- Lebonnois, S., Sugimoto, N., & Gilli, G. 2016, *Icar*, **278**, 38
- Lee, S.-H., Reeves, J. M., Wilson, J. C., et al. 2003, *Sci*, **301**, 1886
- Lee, Y. J., Imamura, T., Schröder, S. E., & Marcq, E. 2015a, *Icar*, **253**, 1
- Lee, Y. J., Sagawa, H., Haus, R., et al. 2016, *JGRE*, **121**, 1737
- Lee, Y. J., Titov, D. V., Ignatiev, N. I., et al. 2015b, *P&SS*, **113**, 298
- Lee, Y. J., Yamazaki, A., Imamura, T., et al. 2017, *AJ*, **154**, 44
- Limaye, S. S., Mogul, R., Smith, D. J., et al. 2018, *AsBio*, **18**, 1181
- Limaye, S. S., & Suomi, V. E. 1981, *J. Atmospheric Sci.*, **38**, 1220
- Lovejoy, E. R., Curtius, J., & Froyd, K. D. 2004, *JGRD*, **109**, D08204
- Luginin, M., Fedorova, A., Belyaev, D., et al. 2016, *Icar*, **277**, 154
- Marcq, E., Belyaev, D., Montmessin, F., et al. 2011, *Icar*, **211**, 58
- Marcq, E., Bertaux, J.-L., Montmessin, F., & Belyaev, D. 2013, *NatGe*, **6**, 25
- Markiewicz, W. J., Titov, D. V., Limaye, S. S., et al. 2007, *Natur*, **450**, 633
- McEwen, A. S. 1986, *JGR*, **91**, 8077
- Migliorini, A., Grassi, D., Montabone, L., et al. 2012, *Icar*, **217**, 640
- Mills, F. P., Esposito, L. W., & Yung, Y. L. 2007, in *Exploring Venus as a Terrestrial Planet*, ed. L. Esposito, E. R. Stofan, & T. E. Cravens (Washington, DC: American Geophysical Union), 73
- Molaverdikhani, K., McGouldrick, K., & Esposito, L. W. 2012, *Icar*, **217**, 648
- Nakamura, M., Imamura, T., Ishii, N., et al. 2016, *EP&S*, **68**, 75
- Nakamura, M., Kawakatsu, Y., Hirose, C., et al. 2014, *AcAau*, **93**, 384
- Nordheim, T. A., Dartnell, L. R., Desorgher, L., Coates, A. J., & Jones, G. H. 2015, *Icar*, **245**, 80
- Ogohara, K., Takagi, M., Murakami, S.-y., et al. 2017, *EP&S*, **69**, 167
- Palmer, K. F., & Williams, D. 1975, *ApOpt*, **14**, 208
- Parkinson, C. D., Gao, P., Esposito, L., et al. 2015, *P&SS*, **113**, 226
- Peralta, J., Sánchez-Lavega, A., López-Valverde, M. A., Luz, D., & Machado, P. 2015, *GeoRL*, **42**, 705
- Pérez-Hoyos, S., Sánchez-Lavega, A., García-Muñoz, A., et al. 2018, *JGRE*, **123**, 145
- Pollack, J. B. 1967, *Icar*, **7**, 42
- Pollack, J. B., Dalton, J. B., Grinspoon, D., et al. 1993, *Icar*, **103**, 1
- Rossow, W. B., del Genio, A. D., & Eichler, T. 1990, *JATs*, **47**, 2053
- Rothman, L. S., Gordon, I. E., Babikov, Y., et al. 2013, *JQSRT*, **130**, 4
- Rothman, L. S., Gordon, I. E., Barber, R. J., et al. 2010, *JQSRT*, **111**, 2139
- Shalygina, O. S., Petrova, E. V., Markiewicz, W. J., Ignatiev, N. I., & Shalygin, E. V. 2015, *P&SS*, **113**, 135
- Shkuratov, Y., Kaydash, V., Korokhin, V., et al. 2011, *P&SS*, **59**, 1326
- Sromovsky, L. A., Fry, P. M., Baines, K. H., & Dowling, T. E. 2001, *Icar*, **149**, 435
- Stephens, G. L., O'Brien, D., Webster, P. J., et al. 2015, *RvGeo*, **53**, 141
- Tellmann, S., Häusler, B., Hinson, D. P., et al. 2012, *Icar*, **221**, 471
- Titov, D. V., Bullock, M. A., Crisp, D., et al. 2007, in *Exploring Venus as a Terrestrial Planet*, ed. L. Esposito, E. R. Stofan, & T. E. Cravens (Washington, DC: American Geophysical Union), 121
- Titov, D. V., Markiewicz, W. J., Ignatiev, N. I., et al. 2012, *Icar*, **217**, 682
- Tomasko, M. G., Doose, L. R., Smith, P. H., & Odell, A. P. 1980, *JGR*, **85**, 8167
- Watson, R., & Rothman, L. 1992, *JQSRT*, **48**, 763
- Wilquet, V., Fedorova, A., Montmessin, F., et al. 2009, *JGRE*, **114**, E00B42
- Wu, C. Y. R., Yang, B. W., Chen, F. Z., et al. 2000, *Icar*, **145**, 289
- Yamazaki, A., Yamada, M., Lee, Y. J., et al. 2018, *EP&S*, **70**, 23
- Zasova, L. V., Ignatiev, N., Khatuntsev, I., & Linkin, V. 2007, *P&SS*, **55**, 1712